

2014 iAREA campaign on aerosol in Spitsbergen – Part 2: Optical properties from Raman-lidar and in-situ observations at Ny-Ålesund



C. Ritter^{a,*}, R. Neuber^a, Alexander Schulz^a, K.M. Markowicz^b, I.S. Stachlewska^b, J. Lisok^b, P. Makuch^c, P. Pakszys^{c,d}, P. Markuszewski^{c,d}, A. Rozwadowska^c, T. Petelski^c, T. Zielinski^{c,d}, S. Becagli^e, R. Traversi^e, R. Udisti^e, M. Gausa^f

^a Alfred Wegener Institute, Helmholtz Centre for Polar and Marine Research, Potsdam, 14473, Germany

^b Institute of Geophysics, Faculty of Physics, University of Warsaw, Warsaw, 02-093, Poland

^c Institute of Oceanology, Polish Academy of Sciences, Sopot, 81-712, Poland

^d Centre for Polar Studies National Leading Research Centre, 41-200, Sosnowiec, Poland

^e Department of Chemistry, University of Florence, Sesto F.no, FI, I-50019, Italy

^f Andoya Space Center, Andenes, N-8483, Norway

HIGHLIGHTS

- Temporal evolution of aerosol properties was relatively small.
- Moderate lidar ratios around 30sr–50sr were found.
- The variability in extinction and lidar ratio is larger than in backscatter.
- The lidar ratio is neither correlated to the shape nor the size of the aerosol.
- Two regimes with β^{aer} larger or smaller $1 \text{ Mm}^{-1} \text{ sr}^{-1}$ could be distinguished.

ARTICLE INFO

Article history:

Received 11 November 2015

Received in revised form

18 May 2016

Accepted 26 May 2016

Available online 27 May 2016

Keywords:

Aerosol

Optical properties

Lidar

Lidar ratio

Arctic atmosphere

ABSTRACT

In this work multi wavelength Raman lidar data from Ny-Ålesund, Spitsbergen have been analysed for the spring 2014 Arctic haze season, as part of the iAREA campaign. Typical values and probability distributions for aerosol backscatter, extinction and depolarisation, the lidar ratio and the color ratio for 4 different altitude intervals within the troposphere are given. These quantities and their dependencies are analysed and the frequency of altitude-dependent observed aerosol events are given. A comparison with ground-based size distribution and chemical composition is performed. Hence the aim of this paper is to provide typical and statistically meaningful properties of Arctic aerosol, which may be used in climate models or to constrain the radiative forcing. We have found that the 2014 season was only moderately polluted with Arctic haze and that sea salt and sulphate were the most dominant aerosol species. Moreover the drying of an aerosol layer after cloud disintegration has been observed. Hardly any clear temporal evolution over the 4 week data set on Arctic haze is obvious with the exception of the extinction coefficient and the lidar ratio, which significantly decreased below 2 km altitude by end April. In altitudes between 2 and 5 km the haze season lasted longer and the aerosol properties were generally more homogeneous than closer to the surface. Above 5 km only few particles were found. The variability of the lidar ratio is discussed. It was found that knowledge of the aerosol's size and shape does not determine the lidar ratio. Contrary to shape and lidar ratio, there is a clear correlation between size and backscatter: larger particles show a higher backscatter coefficient.

© 2016 The Authors. Published by Elsevier Ltd. This is an open access article under the CC BY license (<http://creativecommons.org/licenses/by/4.0/>).

1. Introduction

The Arctic region is very sensitive to climate change. Global temperature oscillations occur there with increased amplitude, a

* Corresponding author.

E-mail address: Christoph.Ritter@awi.de (C. Ritter).

phenomenon that is called Arctic Amplification (Serreze and Francis, 2006). Next to the occurrence of feedback mechanisms (e.g. ice – albedo feedback or sea ice thickness, Screen and Simmonds, 2010) also temperature effects (Pithan and Mauritsen, 2014) may contribute to Arctic Amplification.

Aerosol concentration is generally low in the Arctic region (Toledano et al., 2012; Tomasi et al., 2015). However, due to the high surface albedo radiative forcing due to absorbing aerosol may be more positive compared to lower latitudes (Shindell and Faluvegi, 2009). Moreover, radiative forcing of aerosol, both on ground and top of atmosphere, depend not only on the aerosol properties themselves but also on albedo and solar incident angle, can impact atmospheric stability and cloud formation (Stone et al., 2008). Sometimes the effects of aerosol in the atmosphere “dimming” and on ground by reduction of snow or ice albedo by absorbing aerosol which is referred to as “darkening” are distinguished (Stone et al., 2014).

The annual maximum concentration of aerosol in the accumulation mode, that is likely to have an impact on the radiative budget, occurs in the Arctic in springtime, this is known as Arctic haze (Quinn et al., 2007; Yamanouchi et al., 2005). The haze season ends late spring with rising moisture which favors scavenging (Garrett et al., 2011). As the European Arctic atmosphere is influenced by warm Atlantic ocean water, it is not surprising that Arctic haze seems to be less pronounced in Spitsbergen compared to the Canadian Arctic, which is in agreement with results from 2009 PAMARCMIP campaign (Stone et al., 2010). For this reason one can speculate whether the light or moderate aerosol concentrations measured in Spitsbergen nowadays can give a preview to conditions in the Russian or American Arctic in the future in a warming scenario.

Lidar is a mature technology for retrieval of many environmental parameters (e.g. Weitkamp, 2005) and also for aerosol research (Müller et al., 2007). In Spitsbergen currently two Raman-lidar systems for tropospheric aerosol research are operational in long-term projects: the Raman-lidar at the Polish station in Hornsund (77.0N, 15.5E, Karasinski et al., 2014) and the “Koldewey Aerosol Raman Lidar” KARL at Ny-Ålesund (78.9N, 11.9E, Hoffmann et al., 2009). Recently data from KARL has been analysed for 2013 which showed that during spring the aerosol depolarisation (measure of the scatterers’ asphericity) is increased and posed the question, whether the lidar ratio underlies an annual cycle (Tomasi et al., 2015).

For climate models which include an active aerosol module or simply for judging the radiative impact of aerosol, its properties and vertical distribution must be known with error estimation from observations. So far only few height resolved data on Arctic aerosol exist that either describe case studies (e.g. Stock et al., 2012) or lidar profiles with coarse monthly averages (Tomasi et al., 2015). For this reason in this work data from the Ny-Ålesund lidar is used to provide, to our knowledge for the first time, a complete statistics on lidar derived aerosol parameters. The period between 26 March and 29 April 2014 is analysed in detail. During this time further aerosol measurements, both in-situ and from sun photometers, have been performed in Ny-Ålesund and at the local capital Longyearbyen (78.2N, 15.6E) in the frame of the “iAERA” project (Impact of absorbing aerosols on radiative forcing in the European Arctic) (Lisok et al., 2016; paper 1). In that work for a number of cases a comparison between ground-based, in-situ aerosol measurements on the one hand and lidar and sun photometer data on the other hand have been compared. One of the findings was that due to the complexity of the orography (and hence the boundary layer behaviour) in Spitsbergen no easy correlation between aerosol properties on the ground and in the column could be drawn. Therefore in this work averages over short periods of time are

considered, which may be more comparable among different instruments and more representative for the site. For this reason the data presented here could be used more easily for comparison with models. Moreover, our approach is easily feasible for other Raman-lidar data at different sites.

In section 2 the instruments and evaluation schemata are briefly introduced, in section 3 the results are given from ground-based (3.1) and remote sensing (3.2–3.4) observations. In section 4 the main findings are discussed, which includes the observation of a drying aerosol layer that has been activated by a cloud.

2. Data and evaluation methods

KARL is a “ $3\beta+2\alpha+2\delta+2wv$ ” Raman-lidar, which means that in 3 colors (355 nm, 532 nm and 1064 nm) the backscatter coefficient (β) is measured, in 2 colors (355 nm and 532 nm) the extinction coefficient (α), in 2 colors (355 nm and 532 nm) the depolarisation (δ) and in another 2 colors (407 nm, 660 nm) the water vapor (wv). It consists of a 70 cm detection mirror, working at a field of view of 1.75 mrad and a 50 Hz Nd:Yag laser which emits about 10 W for each of the aforementioned three wavelengths. More technical information is provided in Hoffmann 2011. KARL is located in the atmospheric observatory in research village of Ny-Elesund at the West coast of Spitsbergen. The region is orographically strongly divided into a fjord in the North (open water during the campaign) and up to 1000 m high mountains to the South, East and North of the site. As the surface temperatures remained below 0 °C during the iAREA campaign, the ground was fully covered by snow. However, it must be noted that due to the warm Westspitsbergen current the temperatures at the whole West coast of Spitsbergen are quite mild for the given latitude.

The lidar data for the extinction coefficients and for the backscatter coefficients at 355 nm and 532 nm have been evaluated according to Ansmann et al. (1992), the backscatter coefficient for the infrared (1064 nm) has been evaluated according to Klett 1981, with an assumed lidar ratio $LR = 30$ sr (see below). To derive the aerosol backscatter coefficients with both methods and to subtract the Rayleigh contribution of backscattering and extinction, air density profiles obtained from radiosonde data from the site have been used. In Ny-Ålesund daily at UT 11 a Vaisala RS-92 has been launched. Moreover, a calibration is required for the retrieval of the backscatter coefficient in both methods. As only clear sky measurements have been evaluated here we had a sufficient signal to noise ratio (SNR) in the low stratosphere, which was apparently clean. Hence, clear sky conditions have been assumed there, by setting in 13 km altitude: $\beta^{\text{aer}}(532 \text{ nm}) = 0.05 \cdot \beta^{\text{Ray}}(532 \text{ nm})$ and an Ångström exponent for the aerosol backscatter of -1 (Ångström, 1929).

All data were evaluated with 30 m vertical and 10 min temporal resolution without any further smoothing or filtering. For this work not only cloud contaminated profiles (possible multi scattering) but also profiles with inhomogeneous technical settings (different overlap functions) have been removed. At the end 454 lidar profiles (each corresponding to 10 min) for 17 different days with observations between March 26 and April 29, 2014 remained.

From the lidar data the following three intensive quantities, which do not depend on the aerosol concentration, the aerosol depolarisation δ , color ratio CR and lidar ratio LR have been derived like this: The aerosol depolarisation δ was calculated from the ratio of the backscattered light in the plane of polarisation parallel to the laser (β_{\parallel}) and the component with perpendicular polarisation (β_{\perp}) according to Freudenthaler et al., 2009.

$$\delta^{aer}(\lambda) = \frac{\beta_{\perp}^{aer}(\lambda)}{\beta_{\parallel}^{aer}(\lambda)} \quad (1)$$

This depolarisation is a measure of the particles' shape as spherical scatterers do not show any depolarisation. Further we define the color ratio CR as:

$$CR(\lambda_1, \lambda_2) = \frac{\beta_{\lambda_1}^{aer}}{\beta_{\lambda_2}^{aer}} \quad (2)$$

This CR is, similar to the Ångström (Ångström, 1929) exponent, a rough estimate of the particle size. Finally the lidar ratio LR is defined as the ratio between aerosol extinction and aerosol backscatter coefficients:

$$LR(\lambda) = \frac{\alpha^{aer}(\lambda)}{\beta^{aer}(\lambda)} \quad (3)$$

The LR is mainly depending on the refractive index, and hence the chemical composition of the aerosol, but also on size (larger for small aerosol, Doherty et al., 1999; Ferrare et al., 2001) and shape (larger for non-spherical particles, Michshenko et al., 1997).

Finally from the lidar returns of 387 nm and 407 nm the water vapor mixing ratio was calculated according to Whiteman et al. (1992), using the radiosonde on site for calibration. Due to the fact that the radiosonde drifts with the wind and our site is directly located at a fjord a calibration uncertainty of 10% even for contemporaneous lidar and sonde observation was taken into account. This uncertainty also includes possible errors in the humidity from the RS-92 radiosonde (Miloshevich et al., 2009).

The Arctic aerosol analysed in this paper was confined to the troposphere. Inspection of the lidar data in altitudes lower than 5 km revealed the following errors: the aerosol backscatter coefficients at 355 nm and 532 nm could be determined to 5% uncertainty, the aerosol backscatter at 1064 nm to 10%, the aerosol extinction coefficient at 355 nm to 50% and aerosol extinction at 532 nm to 100%. The large errors in the extinction are caused by two reasons: First, the retrieval of extinction from lidar data is mathematically an ill-posed problem (Pornsawad et al., 2008). And second in our current set-up the transmission in the Raman shifted 607 nm detection branch, from which the aerosol extinction at 532 nm is calculated (Ansmann et al., 1992), is worse than in the UV. Above 5 km altitude the errors increase further and for this reason no distribution function for the lidar ratio at 532 nm can be presented (it would have been smeared out by noise).

Also temperature profiles from a HATPRO radiometer from Radiometer-Physics, which was continuously operational at the roof of the AWIPEV atmospheric observatory directly in the village of Ny-Ålesund, have been used with the normal software package from the manufacturer.

Direct measurements and aerosol sampling were carried out at the Gruvebadet observatory (about 50 m a.s.l.), located about 500 m South-West from the lidar observatory, during the same field period.

Aerosol size distribution data were obtained from two particle sizers, a Scanning Mobility Particle Sizer (TSI SMPS model 3034) and an Aerodynamic Particle Sizer (TSI APS). Both instruments have been certified by the manufacturer. The calibration system meets ISO-9001:2000, Quality Management Systems-Requirements and complies with ISO 10012:2003, Quality Assurance Requirements for Measuring Equipment. The SMPS-APS integrated system is able to continuously collect two synchronized size spectra every 10 min. SMPS provides a 54 size-classes spectrum in the range 10–487 nm, as a mean of 3 three-minutes measurements; APS gives a 52 size-

classes spectrum in the range of 0.5–20 μm , as an average of 9 one-minute measurements. One minute stop allows the two devices synchronization.

Aerosol samples were continuously collected from 31 March to 18 April with a PM10 (particle matter collected with a 10 μm cut-off head) sampler (TCR TECORA sequential aerosol sampler) at daily resolution (00:01–23:59 UTC) on Teflon filters (Pall, 47 mm diameter, 2 μm nominal porosity). The sampling head was designed according to EN-12341 European rules and operated at 38.3 L min⁻¹ (actual volume), corresponding to a 24 h volume of about 55 m³. Data loss occurred after 18 April due to a system failure.

One half of each PM10 Teflon filter was extracted in about 10 ml MilliQ water (accurately evaluated by weighing) by ultrasonic bath for 20 min for ionic content determination. Inorganic anions and cations were simultaneously measured by Ion-Chromatography. The sample handling during the injection was minimized by using a specifically-designed Flow-Injection Analysis (IC-FIA) device (Morganti et al., 2007). Cations (Na⁺, NH₄⁺, K⁺, Mg²⁺ and Ca²⁺) were determined by using a Dionex CS12A-4 mm analytical column with 20 mM H₂SO₄ eluent. Inorganic anions (Cl⁻, NO₃⁻, SO₄²⁻) were measured by a Dionex AS4A-4 mm analytical column with a 1.8 mM Na₂CO₃/1.7 mM NaHCO₃ eluent. Six standard calibration curves daily were used for quantification. Further details are reported in Becagli et al., 2011.

The aerosol chemical components (sea salt and crustal) were calculated as reported in Udusti et al. (2012). Firstly, the non-sea-salt(nss) and sea salt(ss) fraction of Na⁺ and Ca²⁺ were calculated according to the following equations:

$$\text{ssNa} = \text{Na} - \text{nssNa} = \text{Na} - \text{nssCa} * (\text{Na/Ca})_{\text{crust}}$$

$$\text{nssCa} = \text{Ca} - \text{ssCa} = \text{Ca} - \text{ssNa} * (\text{Ca/Na})_{\text{seawater}}$$

where Na and Ca represent the total concentration measured by ion chromatography in each sample and (Na/Ca)_{crust} and (Ca/Na)_{seawater} represent the element ratios (weight/weight) in the Earth crust and in seawater (0.56 w/w and 0.038 w/w, respectively - Bowen, 1979). Using these ratios and the equations above we find that over the whole 2014 campaign 94.5% of the Na⁺ and 24.9% of Ca²⁺ originates from the sea spray as expected for a marine remote site as Ny-Ålesund.

The amount of sea salt aerosol was calculated as 3.25*ssNa mass (Kerminen et al., 2000) and crustal contribution was calculated by nssCa, considering its percentage in the Earth crust (4.58% w/w, Rudnick and Gao, 2004).

3. Results

Data in this section is analysed for 4 different periods which have been selected such that gaps in the lidar observation due to cloud cover were used to create groups with similar length, giving similar precision in statistical analysis. These 4 periods are: 1) 26 March – 4 April 2) 5 April – 7 April 3) 10 April – 14 April 4) 22 April – 29 April. As the lidar cannot operate in conditions with low clouds storms had to be excluded. The above mentioned four time intervals show quite similar synoptic forcing with prevailing northern winds which were derived by inspection of the ERA-Interim 2×2 Reanalysis data set (Dee et al., 2011). These winds came from NNW during the first two periods. During 10 April to 14 April the synoptic forcing was almost zero with very low wind speeds at 850 hPa around Spitsbergen. During the last period the wind came directly from northern directions. Moreover, for the lidar data we concentrate on aerosol properties mainly in four altitudes: the range from 1 to 1.5 km, 2–2.5 km, 2.5 – 5 km and 5 – 8 km altitude. The lowest interval is definitely above the overlap of

the lidar (Hofmann, 2011), but still in the region of high backscatter in the 2013 data set (Tomasi et al., 2015), see also in Fig. 5. The second interval points already to a higher altitude than the highest mountains in Spitsbergen and hence we expect much less orographic influence in that level. The third interval still has a reasonable SNR for the Raman channels, see previous section, while the highest interval might be interesting as some work indicate high-altitude transport of pollutants into the Arctic (Stohl, 2006). Ground-based in-situ data have been prepared for the same time intervals.

3.1. Ground-based size distribution and chemistry

For later comparison with the lidar data in this section a short overview of ground-based chemical analysis of the aerosol properties is provided. However, due to the complex orography at the site and the quickly varying relative humidity any comparison between ground-based in-situ and lidar data may not lead to the same result. Fig. 1 shows the size distribution spectra and daily chemical composition of atmospheric particulate measured during the 26 March – 4 April period. Both records show some data gaps due to start of the measurements campaign (26 March in the evening for size distribution and 31 March for aerosol sampling).

The largest particle population is present in the accumulation mode (0.1–0.5 μm , SMPS plot), with the highest concentrations on early 27 March, 28 March and especially 4 April. Larger particle (APS plot) show a similar pattern, with the largest values on 28 March and 4 April (slightly shifted toward the end of the day, with respect to the smaller size).

Chemical composition enlightens that the 4 April aerosol is dominated by a large sea spray concentration (3700 ng/m^3), together with a small increase of the nss-sulphate and ammonium contributions. Crustal and nitrate loads are quite constant along all the period, with a lower crustal contribution on 31 March.

Fig. 2 shows the plots for size distribution plots daily chemical composition of atmospheric particulate measured during 5–7 April 2014. Besides a sharp nucleation event on 5 April in the afternoon, SMPS size spectrum shows that the size range 0.1–0.3 μm becomes more and more relevant all along this period.

On the contrary, the dominant mode in the APS measurements (0.7–0.9 μm) shows a larger particle population especially in the first half of the measurement period. This pattern perfectly fits to the chemical composition, showing a progressive increase in sulphate and ammonium concentration (about twofold for both), mainly associated with the finest mode, and a gradual decrease of sea salt (about four times), mainly related to the larger size particles.

Overall the period from 4 April to 7 April showed the highest aerosol concentration of the campaign and its composition was a mixture between sea salt, dominating in the first two days and sulphate, ammonium and crustal elements towards the end of this period.

Fig. 3 shows the available SMPS and APS measurements and chemical composition in the 10–14 April period. Unfortunately, due to technical failures, the data from particle sizers cover only the first two days. Here the particle concentration is lower than before. Only a weak increase of the particle population in the 0.1–0.5 μm range on late 11 April can be highlighted. By looking at the chemical composition, such an increase is likely to be ascribed to an enhancement of both sea salt and sulphate atmospheric concentration during that day.

For the period 12–14 April we can observe a progressive increase, though starting from moderate levels, of the atmospheric concentrations of all the components, with the exception of nitrate contribution, which seems to remain almost constant.

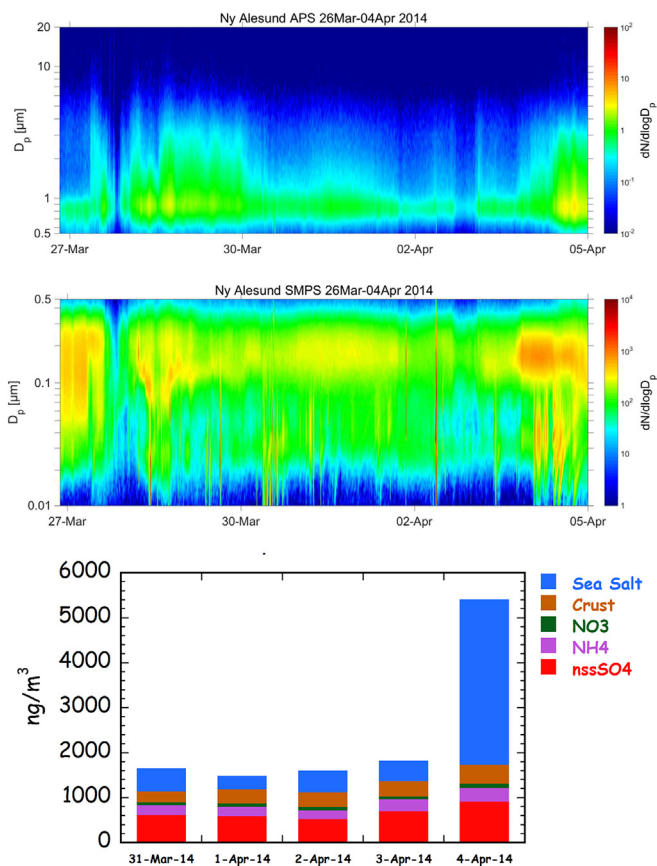


Fig. 1. Size distribution (in the nano-metric and micro-metric range) and chemical composition of atmospheric particulate during the 26 March – 4 April period.

Fig. 4 shows the size distribution plots during the 22–29 April 2014. Unfortunately, the aerosol sampling device crashed during that period and the chemical composition data are not available.

Spectral plots show a low and further decreasing trend for both 0.1–0.5 μm (SMPS) and 0.5–2 μm (APS) particles population from 22 to 29 April. In particular, a low atmospheric load is recorded in late 27 April in the accumulation mode, while an increase of micrometric particles is evident in the late 26 – early 27 April time period.

3.2. Lidar derived overall optical properties

Profiles of the aerosol backscatter coefficient at 532 nm are presented in Fig. 5. The mean profiles for the aforementioned 4 intervals in time are plotted and also the monthly mean of the whole April 2013 for comparison in black. (This latter profile has already been shown in Tomasi et al., 2015). The data sets for the years 2013 and 2014 are comparable as the same cloud screening and evaluation scheme have been applied. It can be seen that, with the exception of the time 5 to 7 April and the lowest 750 m, it was always clearer in the 2014 season. Especially in the free troposphere between 3 and 6.5 km altitude the monthly mean of the aerosol backscatter is only about 60% of the value for the 2013 season.

A detailed overview of the derived values of the aerosol backscatter coefficients β^{aer} [$\text{Mm}^{-1} \text{sr}^{-1}$] for all different altitudes and 532 nm are presented in Figs. 6–9. These probability distributions are quite narrow: in the altitude range from 1 to 1.5 km, values of β^{aer} between 0.3 and 0.6 $\text{Mm}^{-1} \text{sr}^{-1}$ are the most frequent. During beginning of April higher backscatter values have been observed, in

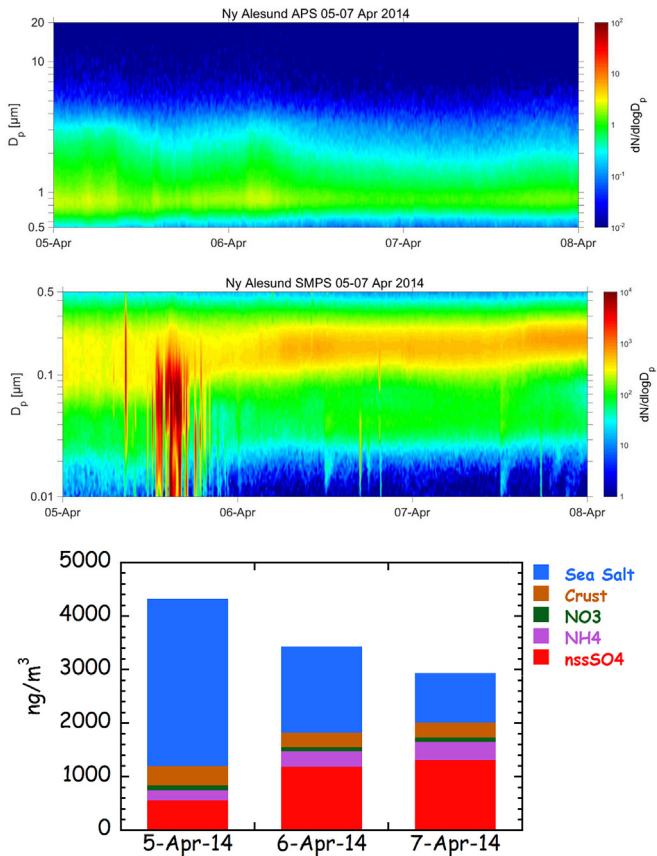


Fig. 2. Size distribution and chemical composition during the 5–7 April period.

agreement the in-situ observations (Fig. 2). However, the decrease of particle concentration at the end of the campaign in the APS and SMPS (Fig. 4) is not very prominent in the backscatter coefficient (blue line). In Fig. 6 also few events with $\beta^{aer} \geq 1 \text{ Mm}^{-1} \text{ sr}^{-1}$ are obvious. We will come back to these later and show that they have intensive quantities which are clearly different to all others. In 2–2.5 km altitude the backscatter drops to $0.15\text{--}0.45 \text{ Mm}^{-1} \text{ sr}^{-1}$ and a temporal trend is not recognisable. In the altitude interval from 2.5 to 5 km backscatter coefficients between 0.05 and $0.25 \text{ Mm}^{-1} \text{ sr}^{-1}$ are most frequent with lower values end of March. Above that (5–8 km, Fig. 9) the air becomes clear and the distribution functions show a sharp peak at only $0.05 \text{ Mm}^{-1} \text{ sr}^{-1}$. Hence we did not find pronounced haze above 5 km altitude. Backscatter coefficients and lidar ratios for typical conditions are also given in the tables in section 3.4. For 355 nm values of β^{aer} between 1.0 and $1.6 \text{ Mm}^{-1} \text{ sr}^{-1}$ (1–1.5 km altitude), $0.6\text{--}1.2 \text{ Mm}^{-1} \text{ sr}^{-1}$ (2–2.5 km altitude), $0.2\text{--}1 \text{ Mm}^{-1} \text{ sr}^{-1}$ (2.5–5 km altitude) and $0.1\text{--}0.3 \text{ Mm}^{-1} \text{ sr}^{-1}$ (5–8 km altitude) have been found while for 1064 nm the corresponding values are $0.05\text{--}0.25 \text{ Mm}^{-1} \text{ sr}^{-1}$, $0.02\text{--}0.2 \text{ Mm}^{-1} \text{ sr}^{-1}$, $0.02\text{--}0.1 \text{ Mm}^{-1} \text{ sr}^{-1}$ and $0.01\text{--}0.05 \text{ Mm}^{-1} \text{ sr}^{-1}$.

The size distribution and chemical composition of the aerosol collected at Gruebadet laboratory (Figs. 1–4) indicate that the higher backscattering values on 5–7 April at the 1000–1500 m altitude could reflect the high contribution of sulphate plus ammonium in the PM10 samples, especially on 7 April, when they cover about 60% of the major ion species. Indeed, the mean atmospheric concentration of sulphate in this period is about 1000 ng/m^3 , with respect to around 700 ng/m^3 and 400 ng/m^3 for the 31 March – 04 April and 10–14 April periods, respectively. This

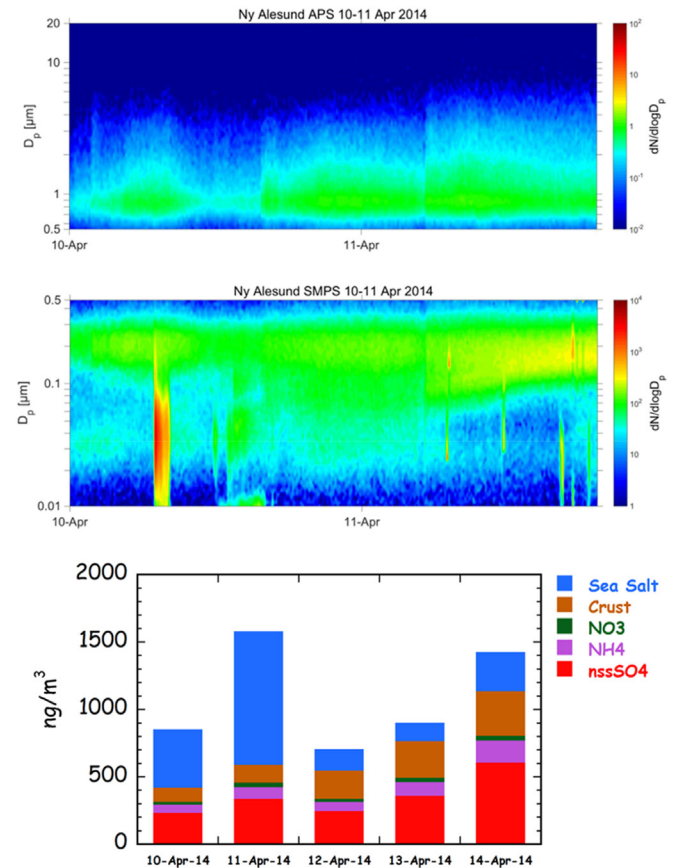


Fig. 3. Size distribution (in the nano-metric and micro-metric range) and chemical composition of atmospheric particulate during the 10–14 April period.

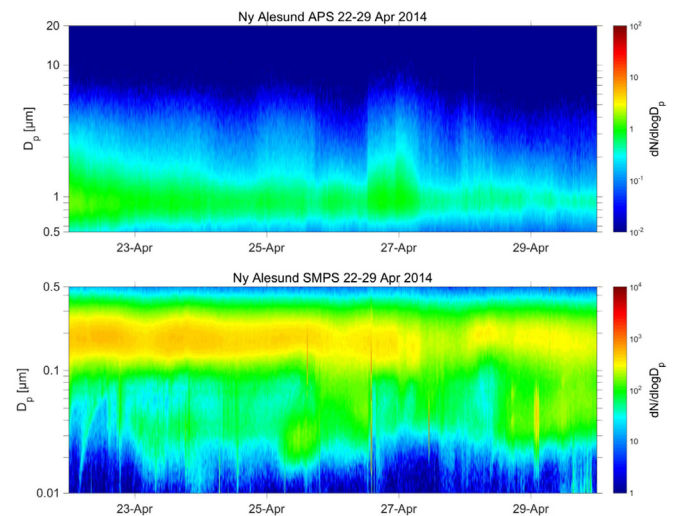


Fig. 4. Size distribution (in the nano-metric and micro-metric range) of atmospheric particulate during the 22–29 April period.

sulphate trend cannot explain the similar backscattering signature recorded for the 26 March – 04 April and 10–14 Apr at 1000–1500 m, 2000–2500 m and 2500–5000 m backscattering pattern, the 2000–2500 m signal for the 5–7 April event is not increased (yellow line), possibly indicating that the aerosol can arrive in

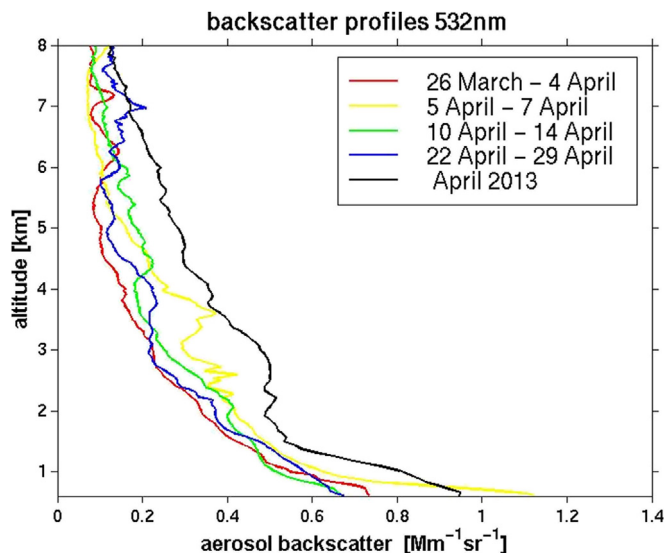


Fig. 5. Profiles of the aerosol backscatter at 532 nm for the 2014 campaign and April 2013.

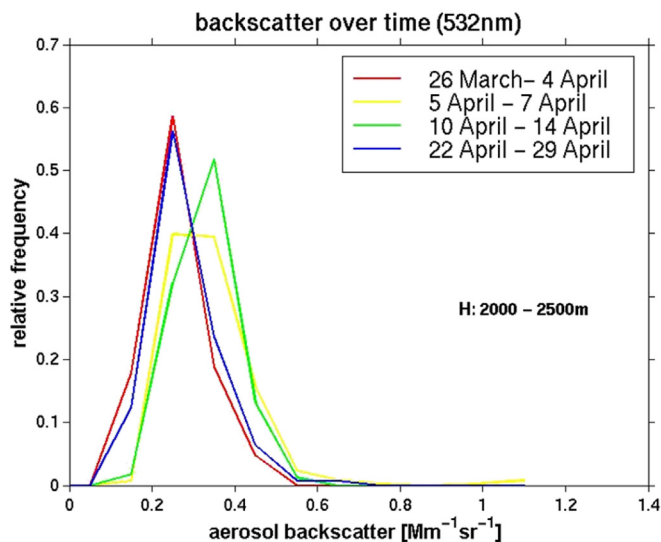


Fig. 7. Aerosol backscatters at 532 nm for the height interval 2–2.5 km altitude.

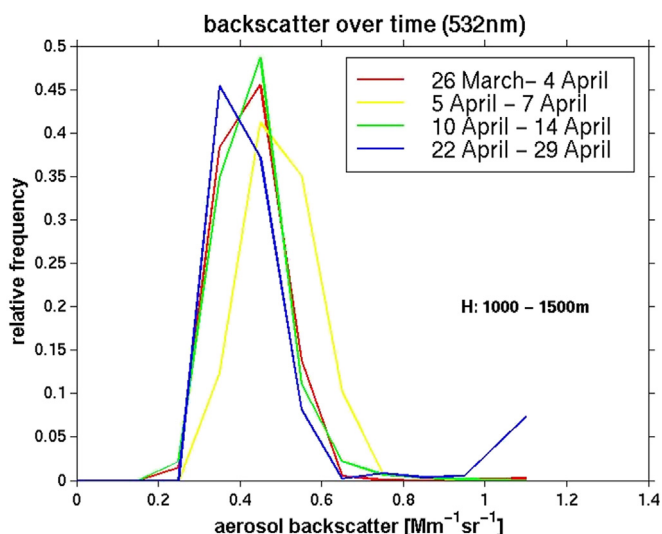


Fig. 6. Aerosol backscatters at 532 nm for the height interval 1–1.5 km altitude.

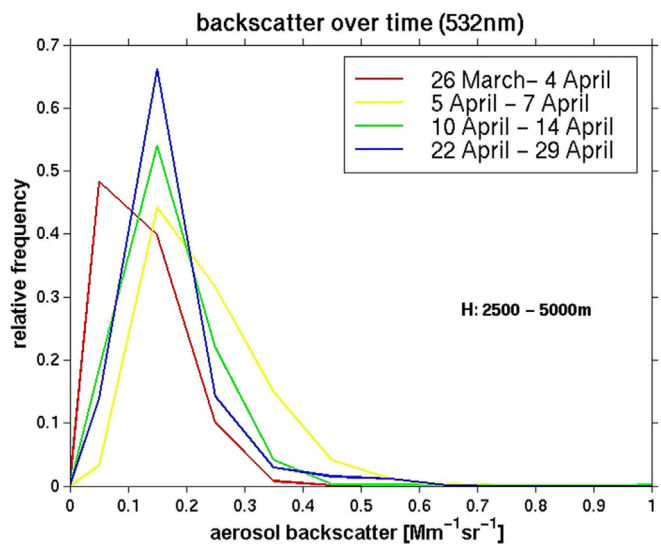


Fig. 8. Aerosol backscatters at 532 nm for the height interval 2.5–5 km altitude.

different distinct layers, making the ground-level measurements less representative for the free troposphere.

In Figs. 10–13 the aerosol extinction coefficients for 355 nm, α^{aer} [Mm^{-1}] for the same altitude intervals as before are shown. Here a broader range of values, from 20 to 90 Mm^{-1} in the lowest altitude interval has been observed. Hence the apparent variability in the extinction coefficient seems to be larger than in the backscatter coefficient. Moreover a clear temporal evolution is apparent, as at the end of the campaign, in the low altitude interval, the extinction drops by about a factor of 2. In the altitudes above 2.5 km the situation is directly opposite as prior to April 4 the extinction is lower by about the same amount. It seems as if the “haze season would start later in high altitudes and vanishes from the ground up”.

The α^{aer} values for 532 nm are not shown for brevity as the same behaviour was found as described before. Values between 3 and 50 Mm^{-1} dominate in the interval 1–1.5 km altitude and again a larger probability of low values after April 22 is obvious. For the interval in 2–2.5 km altitude almost the same extinction values

have been found and again a larger probability of low extinction coefficients at the beginning of the campaign (before 4 April) is observed. In 2.5 km–5 km values between 1 and 20 Mm^{-1} are typical which are again lower at the beginning of the campaign.

The aerosol depolarisation for all height intervals and 532 nm are presented in Figs. 14–17. Moderate depolarisation values around 2–3% are typical below 2.5 km. Above the depolarisation rises slightly with altitude. A possible explanation might be that in higher altitudes (lower temperatures) it is easier for the aerosol to be coated with ice. Also the distribution function appears less broad in 2–2.5 km altitude.

For a comparison of these depolarisation values to the ground-based chemical data it must be noted that only a short lidar observation of April 4 entered in the first data set. Hence, by comparison with Fig. 1 a quite homogeneous chemical composition has been probed by the lidar. Prior to 4 April, the sulphate mean contribution accounts for more than 50% of the total ion-species atmospheric load, taking into account also the ammonium content, often associated to sulphate to give NH_4HSO_4 and $(NH_4)_2SO_4$.

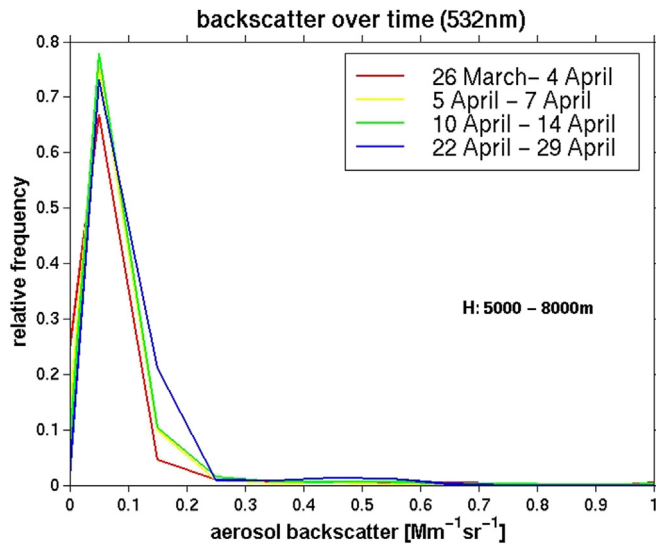


Fig. 9. Aerosol backscatters at 532 nm for the height interval 5–8 km altitude.

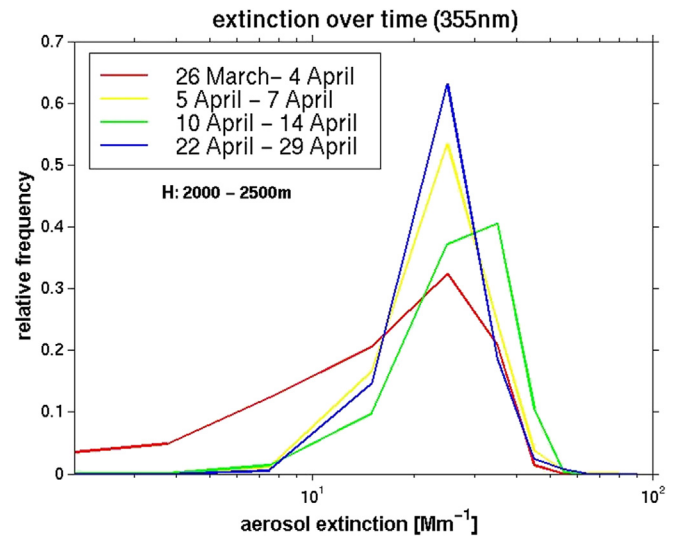


Fig. 11. Aerosol extinction coefficient at 355 nm for the altitude interval 2–2.5 km.

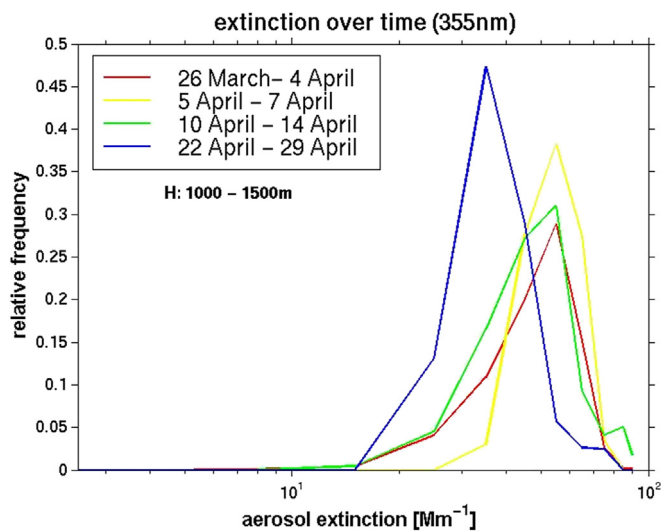


Fig. 10. Aerosol extinction coefficient at 355 nm for the altitude interval 1–1.5 km.

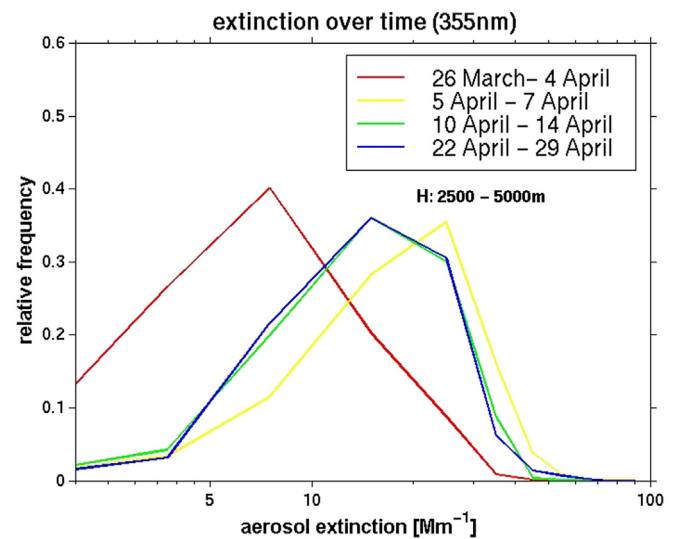


Fig. 12. Aerosol extinction coefficient at 355 nm for the altitude interval 2.5–5 km.

On the contrary, the 5–7 April and 10–14 April events are characterized by high percentage of stronger depolarising (and larger) particles from sea spray and crustal sources. In particular, during 10–14 April two depolarisation modes that could be associated to the large variability in the aerosol chemical composition along the event (Fig. 3) are discernible. The first mode (low depolarisation ratio) could be linked to the relatively high contribution of spherical-like sulphate plus ammonium particles (about 60% of the ion species). On the contrary, the higher depolarisation-ratio mode could be related to the very high contribution of non-spherical sea salt plus crustal particles on 11 April (accounting for about 70% of the ion species load).

The distribution functions of the color ratio are depicted in Figs. 18–21. By definition (eq. (2)) a color ratio of 2 corresponds to an Ångström exponent for the backscatter of approx. 1.7 and a color ratio of 3 to approx. 2.7 (Ångström, 1929). Hence, the observed particles were generally quite small. During the period 26 March–4 April the particles clearly have a different size and show a larger fraction of large particles close to the ground and smaller particles

above 5 km altitude. At 2.5–5 km altitude the aerosol shows the broadest size distribution varies most, while above 5 km altitude larger particles dominate. At the end of the campaign smaller particles are present close to the ground, so in the interval 1–1.5 km the particle size decreases with time.

The comparison of the color ratio to the ground based size distribution gives a fair agreement in that the concentration of particles in the APS range above 0.5 μm gradually decreases during the campaign (Figs. 1–4).

Finally the lidar ratios for 355 nm are plotted in Figs. 22–25. For the low altitude interval here a clear temporal trend is obvious: while at late March/early April lidar ratios $\text{LR} > 70\text{sr}$ did occur, at the end of the campaign only values between 15sr and 42sr had been found. Interestingly this change in LR was only prominent close to the ground and in the 2.5–5 km interval where the LR increased significantly during beginning of April. In the interval 2–2.5 km altitude the probability distributions are again, as the depolarisation, much more narrow, with values between 15 and 50sr for all times. Generally above 2 km altitude there is a weak

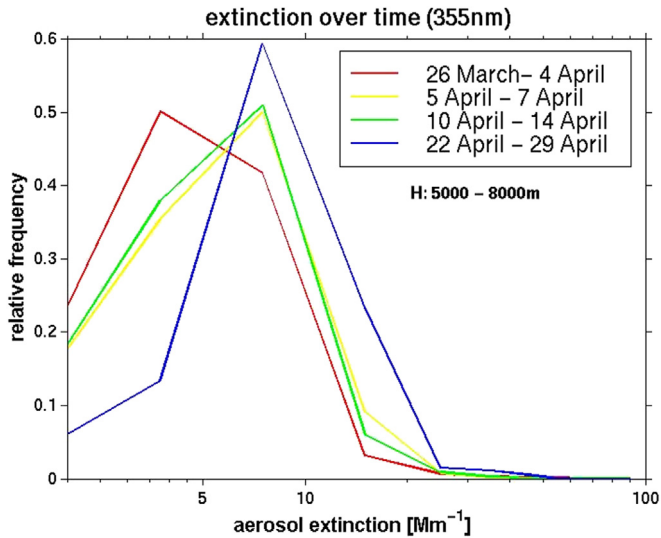


Fig. 13. Aerosol extinction coefficient at 355 nm for the altitude interval 2.5–5 km.

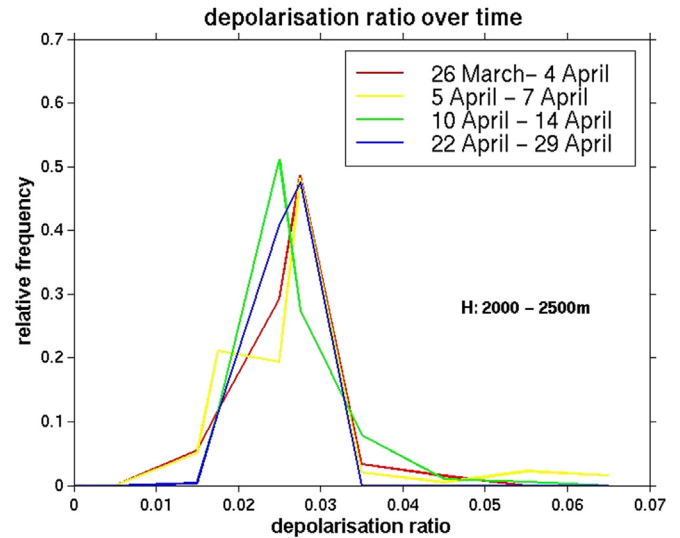


Fig. 15. Aerosol depolarisation at 532 nm for the height interval 2–2.5 km.

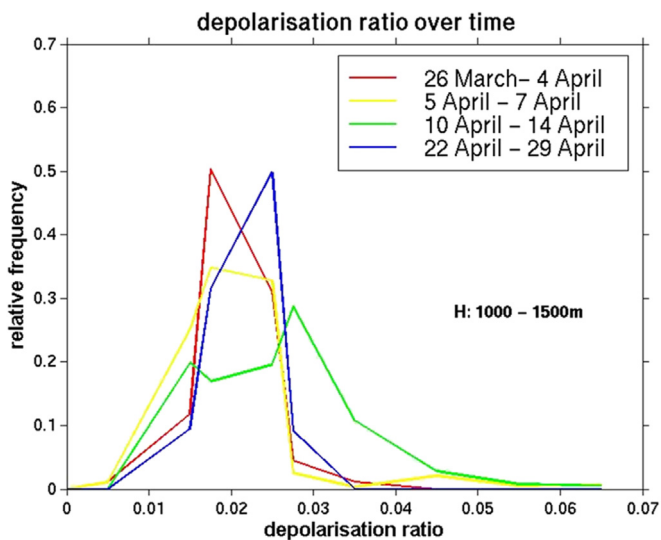


Fig. 14. Aerosol depolarisation at 532 nm for the height interval 1–1.5 km.

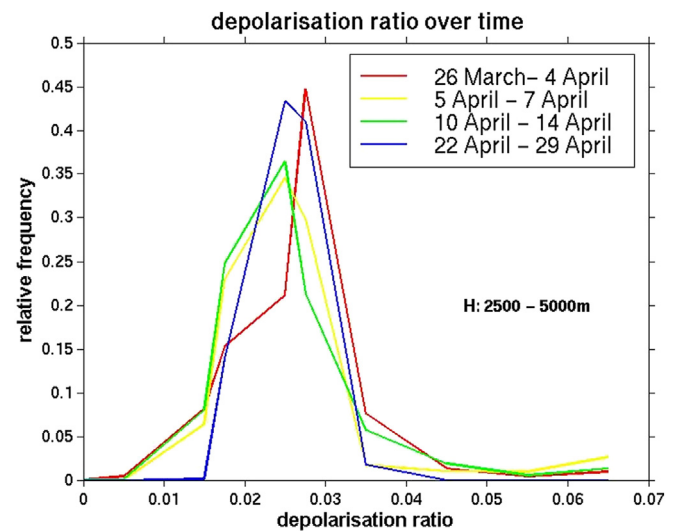


Fig. 16. Aerosol depolarisation at 532 nm for the height interval 2.5–5 km.

tendency for lidar ratios increasing with altitude. The same trend has been reported by Tomasi et al., 2015 for data of the complete year 2013. For 532 nm the LR seems to be principally higher by about 30%, see below in the tables.

The higher lidar-ratios at 1–1.5 km for the 26 March – 4 April period could be justified by higher concentrations of absorbing particles. Indeed, black carbon measurements (A. Lupi, personal communication) by Particle Soot Absorption Photometry (PSAP) show atmospheric concentrations about twice as high with respect to the values measured during the 10–14 April and 22–29 April time periods (we do not have data during 5–7 April due to PSAP failure).

3.3. Relations between the optical parameters

The relation between β^{aer} at 532 nm and the color ratio is given in Fig. 26. Here a clear relation is found: data points with low backscatter coefficients consist of small particles, while large backscatter coefficients are always connected with large particles. It

can also be depicted from Fig. 26 that at the beginning of the campaign the particles were slightly larger (had a lower CR for given β^{aer}). Basically the same relations have been found for other height intervals as well.

The relation between aerosol backscatter and depolarisation is given in Fig. 27. It can be clearly seen that for our data set a value of $\beta^{aer} = 1 \text{ Mm}^{-1} \text{ sr}^{-1}$ is a limit beyond which the depolarisation does not rise to little more than 2%. This indicates that backscatter coefficients larger $1 \text{ Mm}^{-1} \text{ sr}^{-1}$ are related to different, more spherical particles. Note, by comparison to Fig. 14, that the “high depolarisation branches” which look prominent in Fig. 27 consist only of relatively few measurements during the middle of the campaign. Nevertheless for $\beta^{aer} < 1 \text{ Mm}^{-1} \text{ sr}^{-1}$ no clear relation between the shape of the particles and their backscatter has been found.

Next, the relation between the aerosol backscatter and the lidar ratio is presented in Fig. 28. Again a threshold of around $\beta^{aer} = 1 \text{ Mm}^{-1} \text{ sr}^{-1}$ clearly distinguishes two sectors: For smaller backscatter the LR is almost independent of β^{aer} . For larger aerosol backscatter coefficients only low or moderate LR occur. Again here

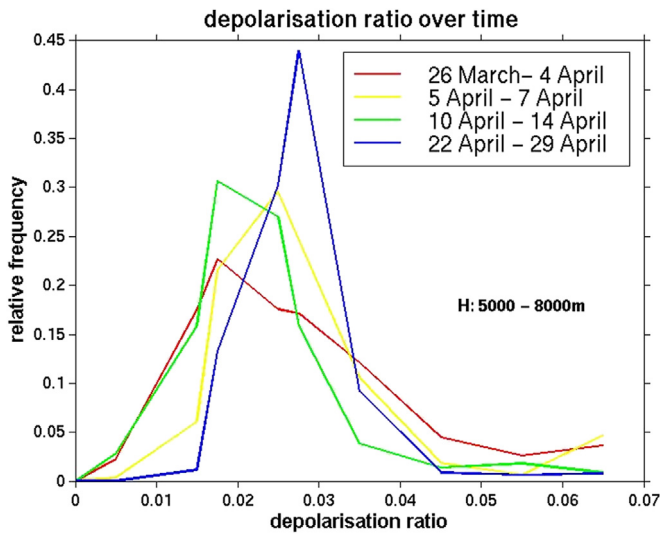


Fig. 17. Aerosol depolarisation at 532 nm for the height interval 5–8 km.

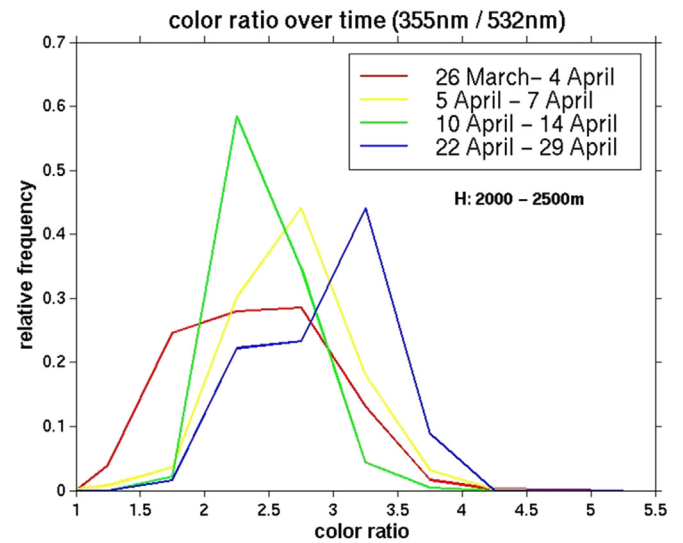


Fig. 19. Color ratio of backscatter between 355 nm and 532 for 2–2.5 km altitude.

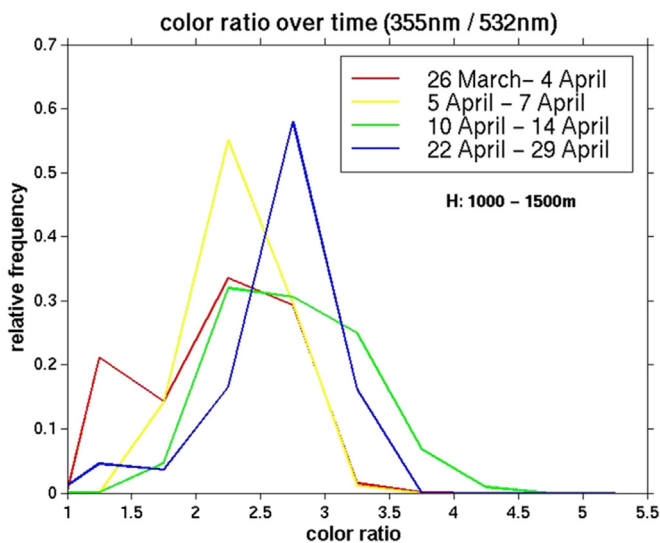


Fig. 18. Color ratio of backscatter between 355 nm and 532 for 1–1.5 km altitude.

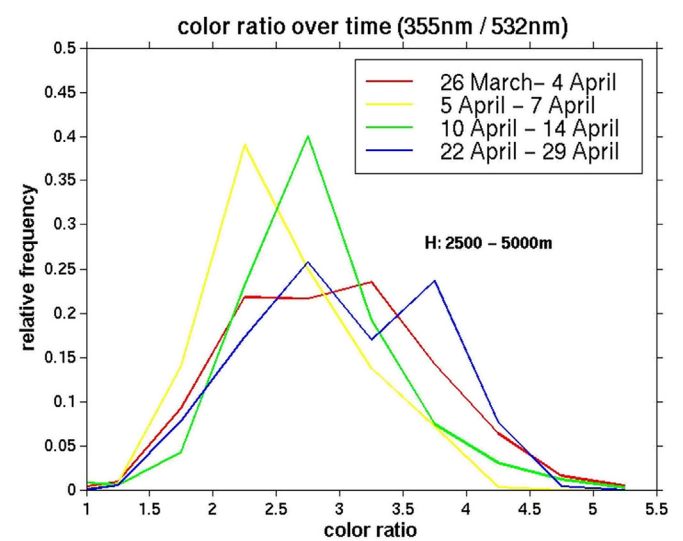


Fig. 20. Color ratio of backscatter between 355 nm and 532 for 2.5–5 km altitude.

as in Fig. 22 it is visualised how the LR at 355 nm decreases over time in the altitude range 1–1.5 km. The dependence of LR with β^{aer} for other altitude intervals is not shown for brevity. However, in agreement to the narrow distribution in Fig. 23, we got the impression that the scatter in LR for given backscatter value was reduced at the end of the campaign as if the particles were more uniform in terms of their microphysics.

Figs. 26 to 28 together indicate that almost every time when β^{aer} at 532 nm was larger than the threshold of $1 \text{ Mm}^{-1} \text{ sr}^{-1}$ the particles have been quite large (color ratio < 1.45), spherical, and consisted of a low or moderate LR. An obvious explanation for these data is that they describe droplets of activated aerosol from subvisible clouds. In section 3.3 one special case will be discussed more detailed.

The relation between the color ratio and the depolarisation is given in Fig. 29, again for the lowest selected height interval. Fig. 29 shows that smaller particles are, in average, stronger depolarising than large particles. Nevertheless high depolarisation values can occur for all but the largest (the “subvisible cloud”) particles. An interesting difference between the larger depolarisation values in

the period 5–7 April consisting from larger particles and the high depolarisation values between 10–14 April consisting of smaller particles can be seen. This might be an effect of the chemical composition measured at ground: In average more sea salt and less crustal aerosol has been found for the earlier period.

Next, in Fig. 30 the same plot of color ratio versus depolarisation for the period April 5 to April 7 and the height interval 1–1.5 km is shown again, but this time resolved for the lidar ratio. It can be seen that the relatively few data points with high depolarisation and $\text{CR} < 2.6$ consist only of particles with small or medium LR (below 50sr). For the main “stripe” and $\text{CR} > 2$ no systematic behaviour is recognisable. In the matrix color ratio, depolarisation, and hence for given size and shape of the particles very different lidar ratios occur. This means that the chemical composition is independent of size and shape for our data. The lidar perceives the particles, with the given resolution of 30 m and 10 min, as if the aerosol were chemically internally mixed. A clear hint of separated soot particles (small size, high depolarisation and lidar ratio) has not been found. Only the few homogeneous data points with large size, large

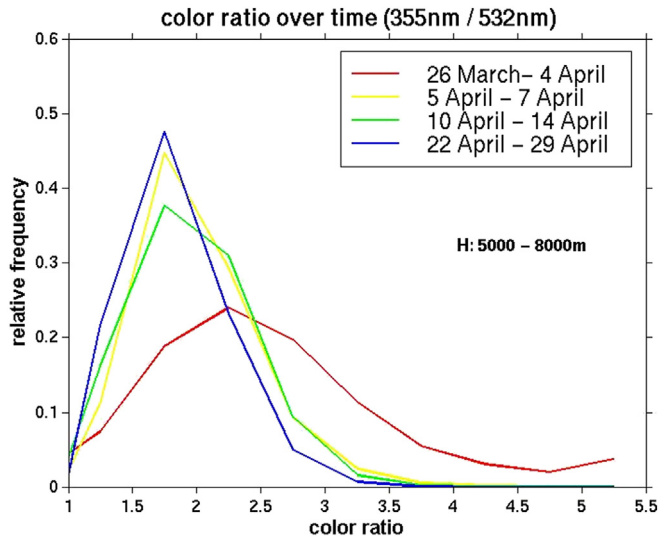


Fig. 21. Color ratio of backscatter between 355 nm and 532 for 5–8 km altitude.

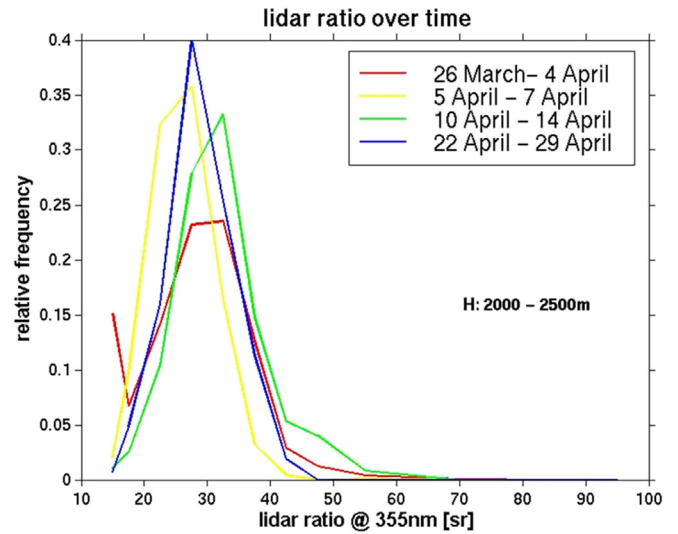


Fig. 23. Lidar ratio at 355 nm for the height range 2–2.5 km.

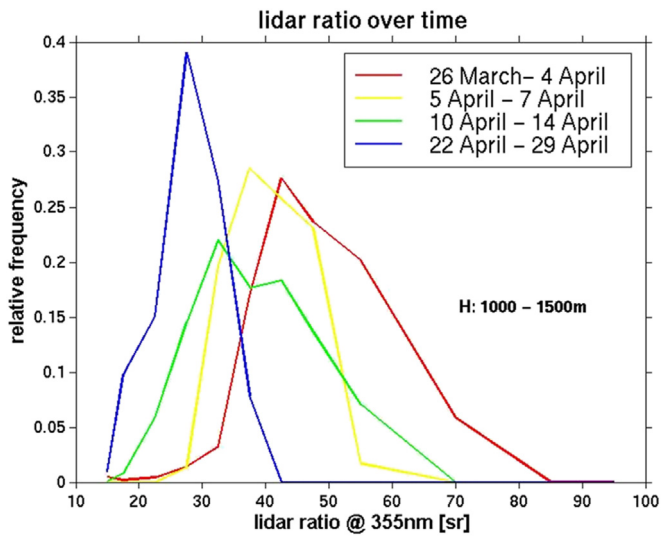


Fig. 22. Lidar ratio at 355 nm for the height range 1–1.5 km.

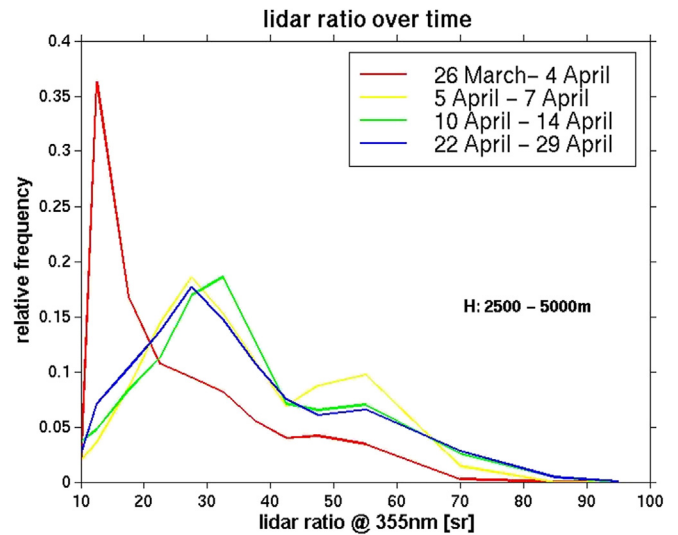


Fig. 24. Lidar ratio at 355 nm for the height range 2–2.5 km.

depolarisation and small to moderate lidar ratio form a distinct data set. Contemporarily at the ground station (Fig. 2 and also paper 1 Lisok et al., 2016) sea salt aerosol has been observed. While under moist conditions sea salt aerosol is surrounded by a shell of water, which should produce only little depolarisation in the lidar, cubic ice crystals under dry conditions show depolarisation values of approx. 10% (Murayama et al., 1999) similar to what is observed here. Nevertheless our lidar data show that these sea salt particles are not the dominant particle species in 1–1.5 km altitude and that the varying lidar ratio from below 20sr–50sr indicates also a chemically diverse composition. So obviously the aerosol types of sulphate, ammonium and crustal aerosol are more dominant aloft.

Finally in Fig. 31 the relation between the color ratio and the lidar ratio is plotted for the altitude interval 1–1.5 km. This figure summarizes some of the results so far: The “drop regime” for $CR < 1.7$ shows decreasing LR with increasing size, as if the large particles had a smaller refractive index, which could simply be explained by water up-take. In the “aerosol regime” with $1.7 < CR < 4.5$ no systematics is visible: at given size the LR might be

large or small. However, the LR decreased over time. Especially at the end of the campaign no cases with $LR > 42sr$ occurred any longer and the particles seemed to become more uniform in size.

3.4. Statistics on the lidar ratio and aerosol occurrences

For many applications, e.g. the evaluation of lidar data for systems which cannot determine the extinction directly, it is important to estimate the lidar ratio as precise as possible. For this reason in this section eight tables (beginning and end of the campaign each for the high and low interval) are presented which show the mean value as well as the 25%, 50% and 75% percentiles of the lidar ratios (LRs) and basic optical properties for different atmospheric cases. According to section 3.2, but otherwise arbitrary, we distinguish the following conditions:

- “clear” $\beta_{532nm}^{aer} < 0.4 Mm^{-1}sr^{-1}$ and $\delta_{532nm}^{aer} < 2.05\%$
- “clear depol” $\beta_{532nm}^{aer} < 0.4 Mm^{-1}sr^{-1}$ and $\delta_{532nm}^{aer} \geq 2.05\%$

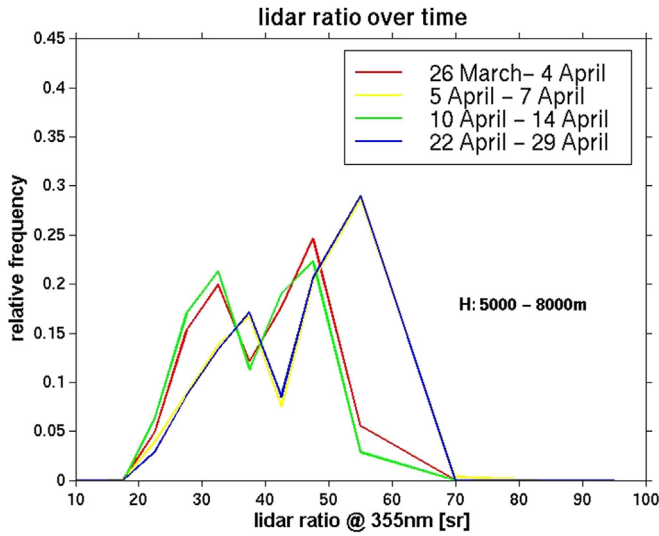


Fig. 25. Lidar ratio at 355 nm for the height range 5–8 km.

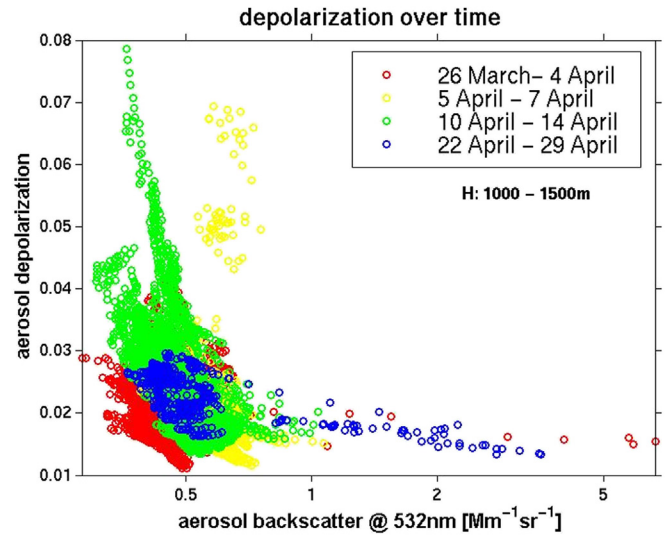


Fig. 27. Relation between aerosol backscatter and depolarisation.

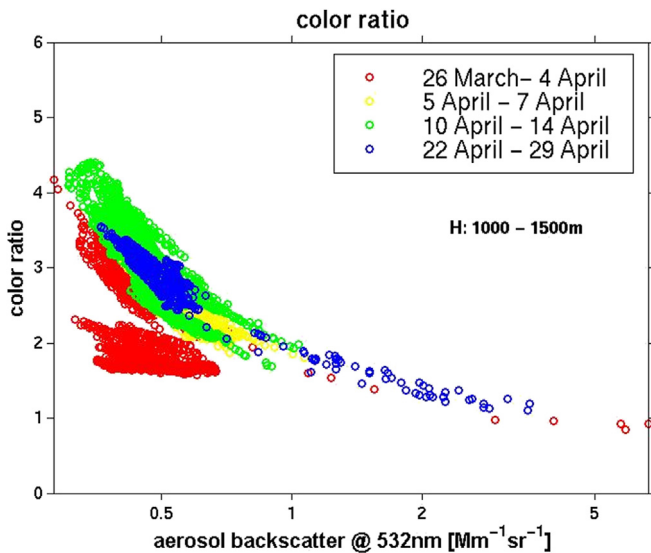


Fig. 26. Relation between aerosol backscatter and color ratio.

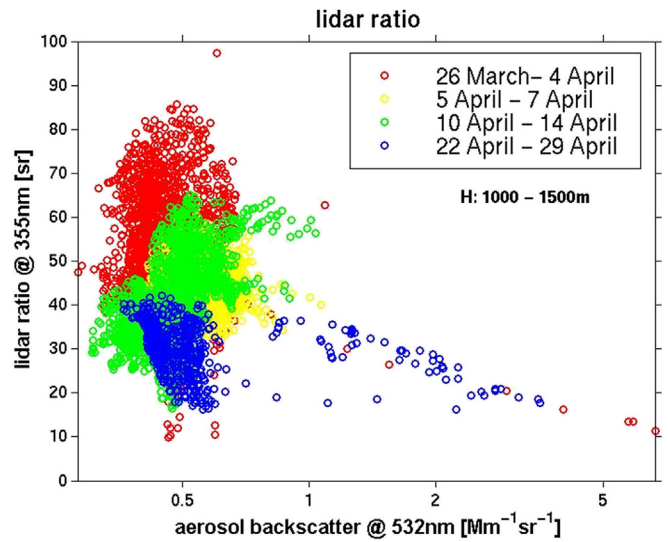


Fig. 28. Relation between aerosol backscatter and lidar ratio.

- c) “spherical aerosol”
 $0.4 \text{ Mm}^{-1} \text{sr}^{-1} \leq \beta_{532\text{nm}}^{\text{aer}} < 1 \text{ Mm}^{-1} \text{sr}^{-1}$ and $\delta_{532\text{nm}}^{\text{aer}} < 2.05\%$
- d) “depol. aerosol”
 $0.4 \text{ Mm}^{-1} \text{sr}^{-1} \leq \beta_{532\text{nm}}^{\text{aer}} < 1 \text{ Mm}^{-1} \text{sr}^{-1}$ and $\delta_{532\text{nm}}^{\text{aer}} \geq 2.05\%$
- e) “activated aerosol”
 $\beta_{532\text{nm}}^{\text{aer}} \geq 1 \text{ Mm}^{-1} \text{sr}^{-1}$ and $\delta_{532\text{nm}}^{\text{aer}} < 2.05\%$ and $CR < 1.7$
- f) “dense aerosol” $\beta_{532\text{nm}}^{\text{aer}} \geq 1 \text{ Mm}^{-1} \text{sr}^{-1}$ and $CR \geq 1.7$

It must be noted that the lidar was operational during all times when the weather allowed observations but that clouds had to be removed from the data. If one assumes that activated aerosol might be located close in space and time to clouds then this would mean that such cases are underrepresented in our study.

The lidar ratios for both colors (355 nm, 532 nm) for the beginning of the campaign and low altitudes are presented in Table 1. It can be seen that for this data set the LRs for 355 nm are slightly higher than for 532 nm. Moreover the LR for the cases “clear depol”, “spherical aerosol” and “depolarising aerosol” are similar with values around 40sr–55sr. The cases of activated

aerosol show considerably lower lidar ratios, especially for the 532 nm. For the 532 nm color it seems that the LRs for the non-spherical particles are slightly but systematically larger than for the spherical particles. Moreover it can be seen that typically the mean value is larger than the 50% percentile meaning that there are a few data points with high LR. To demonstrate the behaviour of the surprisingly low lidar ratio for the activated aerosol cases in more detail we present in Fig. 32 the dependence of the LR on the color ratio. The blue crosses for the 355 nm channel are identical to those presented in Fig. 31. The dependence seems to be systematic: the lowest lidar ratios are found for a color ratio between 0.9 and 1. Moreover the lidar ratios between both colors seem to be correlated. For this reason we do not think that the low values for 532 nm are caused by noise in the data.

The lidar ratios for both colors (355 nm, 532 nm) for the same time and higher (2–2.5 km) altitudes are presented in Table 2. The probability to find aerosol backscatter coefficients below $0.4 \text{ Mm}^{-1} \text{sr}^{-1}$ (“clear”, “clear depol”) is largely increased. Aerosol was found almost entirely with depolarisation values above 2.05%.

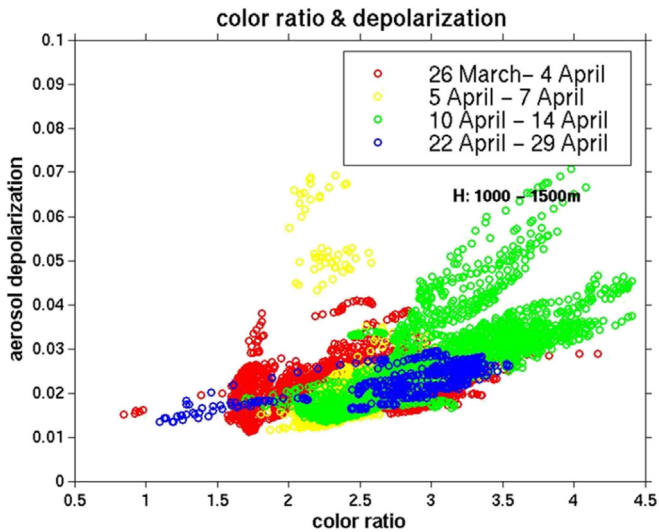


Fig. 29. Dependence of depolarisation at 532 nm from color ratio at 1–1.5 km altitude.

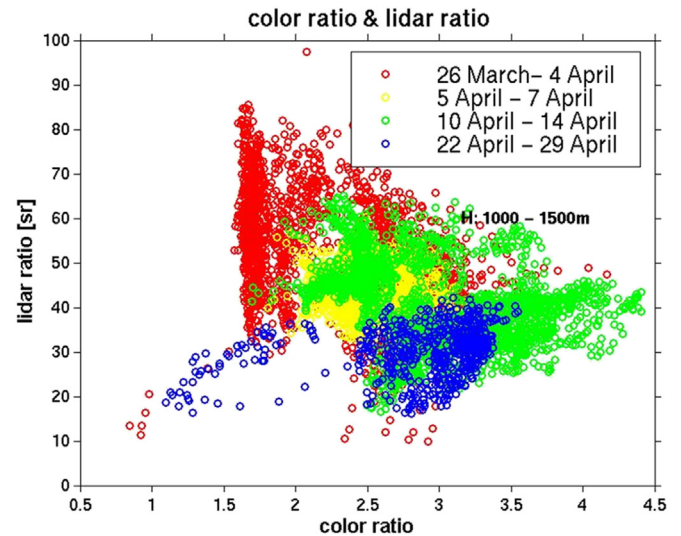


Fig. 31. Color ratio versus lidar ratio at 355 nm for the height interval 1–1.5 km.

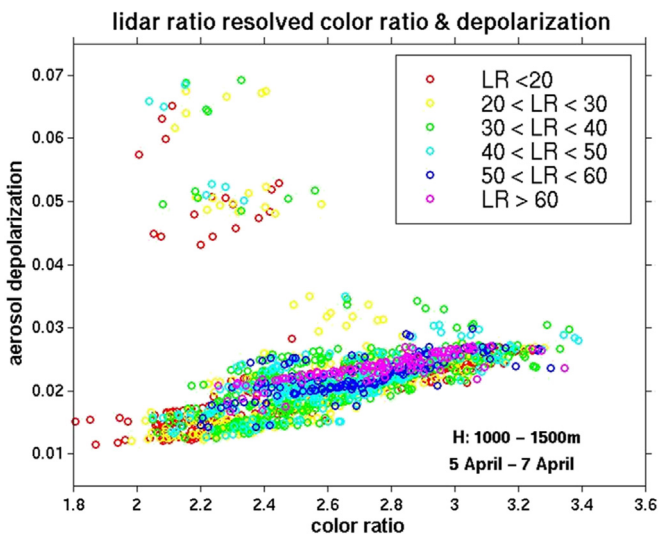


Fig. 30. Relation between color ratio, depolarisation and lidar ratio.

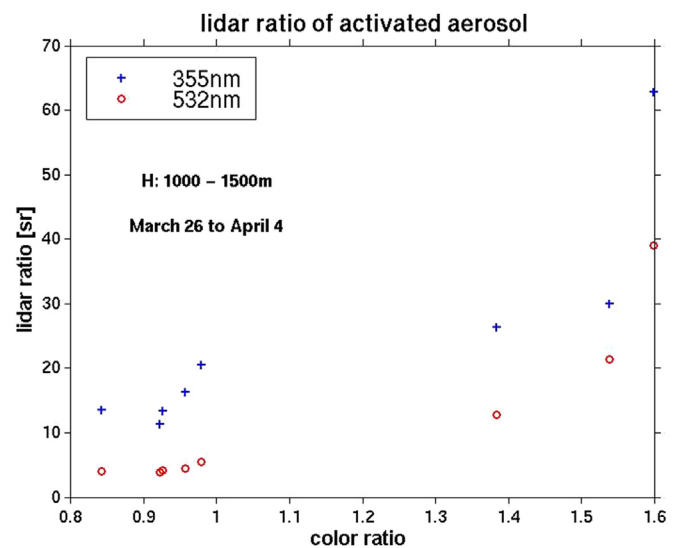


Fig. 32. The lidar ratio for activated aerosol, height: 1–1.5 km from March 26 to April 4.

In this altitude the lowest lidar ratios occur. Moreover, the LR at 532 nm is here overall larger than that for 355 nm and it depends at 532 nm strongly on the presence of depolarisation: if the depolarisation is low also lower values of the LR occur. This effect is not so pronounced for 355 nm as here always the LRs are low. For 355 nm the LRs are slightly higher in the presence of aerosol.

The LRs for the altitudes 2.5–5 km and 5–8 km are presented in Tables 3 and 4 respectively. For both altitudes the LR at 532 nm is larger than for 355 nm. Additionally, for 355 nm no pronounced difference between the LR in clear cases or with aerosol has been found. For 532 nm in altitude 2.5–5 km the LR is even lower for aerosol cases than for clear conditions. Above 5 km the LR for 532 nm gets noisy and we only give mean values for the different cases.

From Table 5 can be seen that during the end of the campaign (22 April to 29 April) the LR at 355 nm was significantly lower than before and showed quite homogeneous values for the different selected classes. However, for the 532 nm wavelength a clear variation of the LR has been found with low values for the spherical aerosol and high values for depolarising aerosol and background.

For non-spherical cases the LR at 532 nm is larger than for 355 nm.

Table 6 Summarizes the occurrence frequency and LR for the 2–2.5 km altitude range at the end of the campaign. Less aerosol cases are detected here. The LRs are similar to those of Table 2 with quite low and similar values around 30–40sr for 355 nm and higher values for the 532 nm. In all, the LR at 532 nm is larger for the “clear” cases and lower for the “aerosol” cases, especially when the particles are spherical in shape.

For the altitudes 2.5–5 km and 5–8 km (Tables 7 and 8) the LR at 355 nm is quite similar for clear and polluted cases with values between 30 and 45sr. For 532 nm the LR is similar and again higher for the non-spherical cases. At high altitudes at 532 nm the LR increases, especially for the “clear depol” cases.

4. Discussion

Comparing the backscatter values in Figs. 5–9 with the monthly averages from the 2013 season at the same site obtained by the same instrument (Tomasi et al., 2015) we find higher values during

Table 1

Lidar ratios and aerosol backscatter for the period March 26 to April 4, height: 1 km–1.5 km. Given are the mean value and the percentiles for 25%, 50% and 75% levels. Units for the lidar ratio are [sr], for the aerosol backscatter [$\text{Mm}^{-1} \text{sr}^{-1}$].

H:1–1.5 km 26 March – 4 April 2975 cases	Frequency	LR (355 nm) [sr] percentiles 25%,50%,75%	LR (532 nm) [sr] percentiles 25%, 50%, 75%	Beta_Aer (355 nm) [$\text{Mm}^{-1} \text{sr}^{-1}$] percentiles 25%, 50%, 75%	Beta_Aer (532 nm) [$\text{Mm}^{-1} \text{sr}^{-1}$] percentiles 25%, 50%, 75%	Beta_Aer (1064 nm) [$\text{Mm}^{-1} \text{sr}^{-1}$] percentiles 25%, 50%, 75%
Clear	3.9%	55.2 46.1, 54.9, 64.2	40.2 32.3, 38.0, 44.2	0.85 0.67, 0.75, 1.07	0.37 0.36, 0.37, 0.39	0.11 0.08, 0.12, 0.14
Clear depol	8.3%	50.0 41.7, 46.7, 57.5	44.3 33.1, 41.3, 54.2	0.99 0.75, 1.10 1.18	0.38 0.37, 0.38, 0.39	0.14 0.09, 0.15, 0.17
Spherical aerosol	34.1%	50.2 43.2, 49.4, 57.3	39.2 27.5, 37.5, 48.5	1.09 0.85, 1.09, 1.32	0.49 0.44, 0.48, 0.53	0.24 0.16, 0.18, 0.27
Depol. aerosol	53.5%	49.6 42.9, 46.3, 53.2	45.0 32.2, 44.8, 56.4	1.22 1.10, 1.31, 1.39	0.49 0.43, 0.49, 0.53	0.29 0.18, 0.22, 0.36
Activatedaerosol	0.3%	24.2 13.4, 18.4, 28.2	11.9 4.0, 4.9, 17.1	3.61 2.02, 3.36, 5.14	3.63 1.39, 3.48, 5.82	3.02 1.23, 3.16, 4.97
Dense aerosol	0.0%	–	–	–	–	–

Table 2

Lidar ratios for the period 26 March to 4 April, height: 2 km–2.5 km. Units for the lidar ratio are [sr], for the aerosol backscatter [$\text{Mm}^{-1} \text{sr}^{-1}$].

H:2–2.5 km, 26 March – 4 April 2800 cases	Frequency	LR (355 nm) [sr] percentiles 25%, 50%, 75%	LR (532 nm) [sr] percentiles 25%, 50%, 75%	Beta_Aer (355 nm) [$\text{Mm}^{-1} \text{sr}^{-1}$] percentiles 25%, 50%, 75%	Beta_Aer (532 nm) [$\text{Mm}^{-1} \text{sr}^{-1}$] percentiles 25%, 50%, 75%	Beta_Aer (1064 nm) [$\text{Mm}^{-1} \text{sr}^{-1}$] percentiles 25%, 50%, 75%
Clear	12.7%	18.6 5.9, 18.8, 33.0	22.8 2.2, 22.5, 44.4	0.51 0.48, 0.50, 0.52	0.26 0.24, 0.26, 0.28	0.05 0.04, 0.05, 0.06
Clear depol	75.5%	28.6 24.7, 30.2, 35.0	60.1 27.5, 55.2, 89.0	0.81 0.53, 0.90, 0.96	0.30 0.26, 0.29, 0.33	0.10 0.06, 0.08, 0.13
Spherical aerosol	0.03%	35.1	31.1	1.10	0.43,	0.16
Aerosol depol.	11.7%	35.2 32.3, 35.4, 37.7	66.6 49.0, 66.0, 84.2	1.10 1.07, 1.10, 1.14	0.45 0.42, 0.47, 0.48	0.18 0.16, 0.18, 0.20
Activatedaerosol	0%	–	–	–	–	–
Dense aerosol	0%	–	–	–	–	–

Table 3

Lidar ratios for the period 26 March to 4 April, height: 2.5 km – 5 km. Units for the lidar ratio are [sr], for the aerosol backscatter [$\text{Mm}^{-1} \text{sr}^{-1}$].

H: 2.5–5 km, 26 March – 4 April 1, 4700 cases	Frequency	LR (355 nm) [sr] percentiles 25%, 50%, 75%	LR (532 nm) [sr] percentiles 25%, 50%, 75%	Beta_Aer (355 nm) [$\text{Mm}^{-1} \text{sr}^{-1}$] percentiles 25%, 50%, 75%	Beta_Aer (532 nm) [$\text{Mm}^{-1} \text{sr}^{-1}$] percentiles 25%, 50%, 75%	Beta_Aer (1064 nm) [$\text{Mm}^{-1} \text{sr}^{-1}$] percentiles 25%, 50%, 75%
Clear	17.1%	23.4 14.6, 18.3, 28.0	40.2 10.7sr, 35.8sr, 73.4sr	0.38 0.31, 0.37, 0.47	0.13 0.09, 0.12, 0.18	0.02 0.02, 0.02, 0.03
Clear depol	82.0%	26.1 15.4, 21.6, 33.7	41.9 22.0, 37.0, 67.4	0.53 0.37, 0.48, 0.74	0.16 0.11, 0.16, 0.22	0.04 0.02, 0.03, 0.06
Spherical aerosol	0%	–	–	–	–	–
Aerosol depol.	0.6%	26.7 17.3, 21.3, 34.3	21.9 4.6, 24.3, 40.3	0.96 0.81, 0.95, 1.08	0.60 0.45, 0.60, 0.71	0.40 0.17, 0.40, 0.55
Activated aerosol	0%	–	–	–	–	–
Dense aerosol	0%	–	–	–	–	–

Table 4

Lidar ratios for the period 26 March to 4 April, height: 5 km – 8 km. Units for the lidar ratio are [sr], for the aerosol backscatter [$\text{Mm}^{-1} \text{sr}^{-1}$].

H: 5–8 km, 26 March – 4 April 1, 7500 cases	Frequency	LR (355 nm) [sr] percentiles 25%, 50%, 75%	LR (532 nm) [sr] percentiles 25%, 50%, 75%	Beta_Aer (355 nm) [$\text{Mm}^{-1} \text{sr}^{-1}$] percentiles 25%, 50%, 75%	Beta_Aer (532 nm) [$\text{Mm}^{-1} \text{sr}^{-1}$] percentiles 25%, 50%, 75%	Beta_Aer (1064 nm) [$\text{Mm}^{-1} \text{sr}^{-1}$] percentiles 25%, 50%, 75%
Clear	34.6%	40.0 32.5, 38.8, 47.3	48.8 ± 20 – – –	0.18 0.14, 0.17, 0.20	0.07 0.06, 0.07, 0.08	0.02 0.02, 0.02, 0.03
Clear depol	62.6%	42.8 35.1, 44.0, 50.2	93.4 ± 20 – – –	0.19 0.14, 0.17, 0.22	0.08 0.05, 0.07, 0.09	0.02 0.01, 0.02, 0.03
Spherical aerosol	0%	–	–	–	–	–
Aerosol depol.	2.7%	36.7 30.6, 34.7, 42.3	34.7 ± 20 – – –	0.61 0.50, 0.58, 0.71	0.60 0.48, 0.59, 0.71	0.09 0.05, 0.07, 0.12
Activated aerosol	0%	–	–	–	–	–
Dense aerosol	0%	–	–	–	–	–

Table 5Lidar ratios for the period 22 April to 29 April, height: 1 km–1.5 km. Units for the lidar ratio are [sr], for the aerosol backscatter [$\text{Mm}^{-1} \text{sr}^{-1}$].

H: 1–1.5 km 22 April – 29 April 612 cases	Frequency	LR (355 nm) [sr] percentiles 25%, 50%, 75%	LR (532 nm) [sr] percentiles 25%, 50%, 75%	Beta_Aer (355 nm) [$\text{Mm}^{-1} \text{sr}^{-1}$] percentiles 25%, 50%, 75%	Beta_Aer (532 nm) [$\text{Mm}^{-1} \text{sr}^{-1}$] Percentiles 25%, 50%, 75%	Beta_Aer (1064 nm) [$\text{Mm}^{-1} \text{sr}^{-1}$] percentiles 25%, 50%, 75%
Clear	0%	–	–	–	–	–
Clear depol	2.2%	38.3 37.2, 37.6, 39.2	76.3 66.5, 78.1, 85.3	1.31 1.30, 1.31, 1.33	0.38 0.37, 0.38, 0.39	0.09 0.09, 0.09, 0.10
Spherical aerosol	16.3%	33.3 31.0, 33.6, 35.6	16.5 4.7, 18.6, 28.9	1.40 1.32, 1.37, 1.43	0.53 0.48, 0.51, 0.54	0.15 0.11, 0.13, 0.17
depol. aerosol	73.7%	29.7 26.4, 30.4 33.1	58.1 20.3, 65.4, 94.2	1.42 1.36, 1.40, 1.45	0.47 0.43, 0.44, 0.51	0.14 0.12, 0.13, 0.15
Activated aerosol	4.1%	24.7 20.4, 25.5, 28.9	12.6 9.4, 12.7, 16.4	2.87 2.57, 2.72, 3.18	2.14 1.68, 2.04, 2.53	2.26 1.74, 2.13, 2.60
Dense aerosol	3.5%	31.9 29.6, 32.1, 34.1	19.4 16.5, 19.0, 22.2	2.13 2.01, 2.06, 2.25	1.19 1.13, 1.20, 1.26	0.95 0.82, 0.96, 1.06

Table 6Lidar ratios for the period 22 April to 29 April, height: 2 km–2.5 km. Units for the lidar ratio are [sr], for the aerosol backscatter [$\text{Mm}^{-1} \text{sr}^{-1}$].

H: 2–2.5 km 22 April – 29 April 576 cases	Frequency	LR (355 nm) [sr] percentiles 25%, 50%, 75%	LR (532 nm) [sr] percentiles 25%, 50%, 75%	Beta_Aer (355 nm) [$\text{Mm}^{-1} \text{sr}^{-1}$] percentiles 25%, 50%, 75%	Beta_Aer (532 nm) [$\text{Mm}^{-1} \text{sr}^{-1}$] percentiles 25%, 50%, 75%	Beta_Aer (1064 nm) [$\text{Mm}^{-1} \text{sr}^{-1}$] Percentiles 25%, 50%, 75%
Clear	4.2%	30.0 26.4, 29.4, 32.5	73.5 55.9, 71.9, 95.0	0.51 0.50, 0.50, 0.52	0.26 0.25, 0.26, 0.27	0.05 0.05, 0.05, 0.06
Clear depol	81.8%	31.0 28.0, 31.0, 34.3	78.6 39.9, 74.3, 114.4	0.50 0.48, 0.50, 0.51	0.26 0.25, 0.27, 0.28	0.06 0.05, 0.06, 0.07
Spherical aerosol	0.8%	35.7 32.3, 33.6, 39.8	29.2 12.2, 29.4, 43.0	0.54 0.54, 0.54, 0.54	0.26 0.25, 0.25, 0.29	0.07 0.06, 0.06, 0.09
Depol. aerosol	13.2%	33.1 28.4, 32.6, 37.1	54.8 38.7, 52.9, 73.5	0.52 0.50, 0.52, 0.54	0.26 0.24, 0.25, 0.28	0.06 0.05, 0.06, 0.07
Activated aerosol	0%	–	–	–	–	–
Dense aerosol	0%	–	–	–	–	–

Table 7Lidar ratios for the period 22 April to 29 April, height: 2.5 km – 5 km. Units for the lidar ratio are [sr], for the aerosol backscatter [$\text{Mm}^{-1} \text{sr}^{-1}$].

H: 2.5 – 5 km 22 April – 29 April 3024 cases	Frequency	LR (355 nm) [sr] percentiles 25%, 50%, 75%	LR (532 nm) [sr] percentiles 25%, 50%, 75%	Beta_Aer (355 nm) [$\text{Mm}^{-1} \text{sr}^{-1}$] percentiles 25%, 50%, 75%	Beta_Aer (532 nm) [$\text{Mm}^{-1} \text{sr}^{-1}$] percentiles 25%, 50%, 75%	Beta_Aer (1064 nm) [$\text{Mm}^{-1} \text{sr}^{-1}$] percentiles 25%, 50%, 75%
Clear	5.4%	31.2 23.4, 30.2, 35.8	29.7 9.7, 34.4, 53.4	0.64 0.55, 0.62, 0.74	0.21 0.16, 0.20, 0.23	0.03 0.02, 0.02, 0.03
Clear depol	91.2%	34.5 24.5, 31.9, 41.6	37.2 20.2, 38.1, 55.2	0.65 0.54, 0.63, 0.76	0.20 0.16, 0.18, 0.22	0.04 0.02, 0.03, 0.05
Spherical aerosol	0.6%	46.8 30.7, 46.4, 62.2	43.7 35.4, 42.0, 57.9	0.94 0.88, 0.94, 0.97	0.53 0.50, 0.52, 0.55	0.19 0.18, 0.19, 0.22
Depol. aerosol	2.7%	41.8 35.4, 41.8, 44.6	37.2 31.7, 38.5, 43.2	1.04 0.88, 1.02, 1.21	0.53 0.46, 0.53, 0.57	0.17 0.15, 0.17, 0.20
Activated aerosol	0%	–	–	–	–	–
Dense aerosol	0%	–	–	–	–	–

Table 8Lidar ratios for the period 26 March to 4 April, height: 5 km – 8 km. Units for the lidar ratio are [sr], for the aerosol backscatter [$\text{Mm}^{-1} \text{sr}^{-1}$].

H: 5–8 km, 26 March – 4 April 1, 7500 cases	Frequency	LR (355 nm) [sr] percentiles 25%, 50%, 75%	LR (532 nm) [sr] percentiles 25%, 50%, 75%	Beta_Aer (355 nm) [$\text{Mm}^{-1} \text{sr}^{-1}$] percentiles 25%, 50%, 75%	Beta_Aer (532 nm) [$\text{Mm}^{-1} \text{sr}^{-1}$] percentiles 25%, 50%, 75%	Beta_Aer (1064 nm) [$\text{Mm}^{-1} \text{sr}^{-1}$] percentiles 25%, 50%, 75%
Clear	34.6%	40.0 32.5, 38.8, 47.3	48.8 ± 20 – – –	0.18 0.14, 0.17, 0.20	0.07 0.06, 0.07, 0.08	0.02 0.02, 0.02, 0.03
Clear depol	62.6%	42.8 35.1, 44.0, 50.2	93.4 ± 20 – – –	0.19 0.14, 0.17, 0.22	0.08 0.05, 0.07, 0.09	0.02 0.01, 0.02, 0.03
Spherical aerosol	0%	–	–	–	–	–
Aerosol depol.	2.7%	36.7 30.6, 34.7, 42.3	34.7 ± 20 – – –	0.61 0.50, 0.58, 0.71	0.60 0.48, 0.59, 0.71	0.09 0.05, 0.07, 0.12
Activated aerosol	0%	–	–	–	–	–
Dense aerosol	0%	–	–	–	–	–

spring 2013 for β^{aer} of 0.7 [$\text{Mm}^{-1} \text{sr}^{-1}$] for the lowest interval and 0.55 [$\text{m}^{-1} \text{sr}^{-1}$] in 2–2.5 km at 532 nm; thus the season in 2014 was apparently clearer by a factor of about 1.6 regarding the backscatter coefficient. Such a pronounced inter-annual variability in the strengths of the haze season in Spitsbergen does occur (Pakszyz et al., 2015). Therefore, unfortunately long time series of observations are required to fully capture all possible aerosol conditions.

The extinction coefficients (Figs. 10 and 13) and hence also the lidar ratio (Tables 1–8) seem to have a larger variability than the backscatter values. For this 2014 season we found frequently only moderate lidar ratios between 30 and 50sr. These values are lower than reported by Müller et al. (2007) for Arctic haze but are much more in agreement to our experience for Ny-Ålesund (Tomasi et al., 2015). One reason could be that the West Coast of Spitsbergen is strongly affected by the Atlantic Ocean and hence a mixture between “marine” and “Arctic” conditions (Table 1 from Müller et al., 2007) must be applied for Ny-Ålesund. This view is supported by the chemical analysis of the Gruebadet station (Figs. 1–4) which generally showed a discernible sea salt component. According to previous work for air masses with possibly less contact to open water as the American Arctic some years ago or airborne campaigns (Quinn et al., 2007; Yamanouchi et al., 2005) nss-SO₄ is the main component of Arctic haze events. Moreover, airborne sun-photometer measurements from Stone et al. (2010) indicate that the Arctic haze phenomenon might generally be less pronounced in the European Arctic compared to colder regions. Frequently and in agreement to unpublished data from previous years we find that LR532 > LR355 for Arctic haze conditions in Ny-Ålesund and that the lidar ratios for haze and background are quite similar, with the exception of the end of our campaign (Fig. 22, Table 5) where only modest lidar ratios for the aerosol have been found.

Generally our lidar derived extinction coefficients are quite high. In the lowest altitude interval from 1 to 1.5 km typical values of 20–70 Mm^{-1} for 355 nm have been found and 3–30 Mm^{-1} for 532 nm. Compared to ground-based in-situ measurements (e.g. paper 1 by Lisok et al.) remote sensing instruments as lidar and photometer seem to overestimate the extinction by a factor of 4. A smaller overestimation of extinction from lidar data, also for Ny-Ålesund, has already been discussed by Tesche et al. (2014). A thorough comparison between different aerosol sensors is definitely needed for the future. From our radio sonde data set we can estimate the relative humidity to analyse whether hygroscopic growth of the aerosol closes the gap between the dry in-situ sampling and the lidar measurements in the real moist atmosphere. However, low RHs were common: Between 0 and 5 km altitude we found an average RH of 47% for the time intervals 1–3 and 37% after 22 April. Only about 1/10 of all data points in the radio sondes showed a humidity larger than 80%. In the interval from 0 to 8 km the average humidity dropped further to 44% (26 March to 14 April) and 32% (22 April to 29 April). Zieger et al. (2010) stated for a fall campaign in Ny-Ålesund that a RH of 85% is required for a scatter enhancement of slightly over 4 compared to dry conditions. However, this might not be required for the data of our campaign: From Figs. 1–4 we see that a typical size of the particles is around 180 nm dry. If this diameter were increased to 240 nm, for refractive indices around 1.5, Mie theory states that the extinction coefficient increases by more than factor 4. Also, wet diameters of around 240 nm are in agreement to our color ratios (Figs. 18–21) and similar to those obtained by inversion of the lidar data at the same site for an Arctic haze case of 2009 (Hoffmann et al., 2012). Hence, to close the gap between the extinction values at ground and in the lidar an increase of particle size by roughly 33% would be required. An important implication of this finding is that in climate modelling even under dry conditions the relative humidity must be known precisely to estimate the direct radiative forcing of aerosol.

The most noticeable aerosol event in this data set occurred during beginning April (4.4. to 7.4.) below 1.5 km altitude (Figs. 1, 2 and 5). This case was already discussed by paper 1 Lisok et al., 2016. They found: a) increased AOD in Ny-Ålesund and a decreased Ångström exponent (larger particles in the atmospheric column), b) dominance of sea salt at the ground station, together with an increase in aerosol size and c) air backtrajectories which show influence of the Arctic Ocean and, possibly, also Siberia. From the lidar we see that this event is confined to the lowest atmospheric layers. In 1–1.5 km altitude the depolarisation ratio (Fig. 14), the color ratio (Fig. 18) and the lidar ratio (Fig. 22) are not increased. This means that above 1 km altitude we do not see aerosol properties during these days, which are completely different to other times. The few data points with high backscatter and depolarisation (Fig. 27) show only small to moderate lidar ratios (Figs. 28 and 29). Such lidar ratios are too low for dust or continental aerosol (Müller et al., 2007), but resemble more sea salt, which, in crystal form, could also explain the measured depolarisation (Murayama et al., 1999). Hence we conclude that no clear event of pure Arctic haze had been observed. The larger AOD and backscatter around 5 April was definitely confined to the lowest 1 km and consisted mostly of sea salt (Fig. 2).

A striking feature is the sporadic occurrence of very low lidar ratio for cases of activated aerosol. We just performed a quick check with Mie calculation http://omlc.org/calc/mie_calc.html to confirm that water droplets of 0.8 μm diameter produce lidar ratios around 6sr at 532 nm and around 12sr at 355 nm. Very low lidar ratios, possibly for similar cases, have been derived by Stachlewska and Ritter (2010) using lidar data with the different two-stream evaluation technique. In principle also specular reflections at horizontally aligned ice crystals produce very low lidar ratios (Hogan et al., 2003) but due to our cloud screening and the missing depolarisation such an explanation is unlikely.

Only moderate depolarisation values between 2% and 3% have been found for the 2014 season. Again, these values are lower than for the 2013 season (Tomasi et al., 2015). In that paper a systematic higher depolarisation in the haze season of 2013 has been reported. Hence, the question to what extent normally backscatter and depolarisation values are correlated remains open. For the 2014 season only the distinction between “spherical aerosol”, “depolarising aerosol” and “activated aerosol” could be made, but no dependence of depolarisation on backscatter has been found.

The relation between backscatter and size (color ratio, Fig. 26) is remarkable. It means that the size strictly determines the aerosol backscatter, not the shape (Fig. 27) nor the chemical composition (Fig. 28). An easy hypothesis would be that humidity is the main constrain and that always if the relative humidity is high the particles start growing hygroscopically thereby increasing their scattering efficiency. However, this simple explanation is difficult to prove. With the lidar also the water vapor mixing ratio can be calculated. The result is depicted in Fig. 33. This shows the same data as Fig. 26 but now resolved into values of H₂O mass mixing ratios (units: g water per kg dry air), derived by the lidar. Unfortunately the hygroscopic growth of particles depends on the relative humidity (e.g. Tang, 1996) and precise temperature profiles would be needed to convert the mixing ratio into relative humidities, which we can only estimate by using temperature profiles from a HATPRO radiometer on the site. This radiometer data generally show quite smooth and not very precise profiles. Nevertheless the plot of the mixing ratio clearly shows that the moister conditions match only to data, where the backscatter is low and the particles are small. Contrary, at dry conditions as well large as small particles have been observed. Especially the cases of the activated aerosol have been observed under dry conditions which mean that these events take place either at low temperatures or on the drying

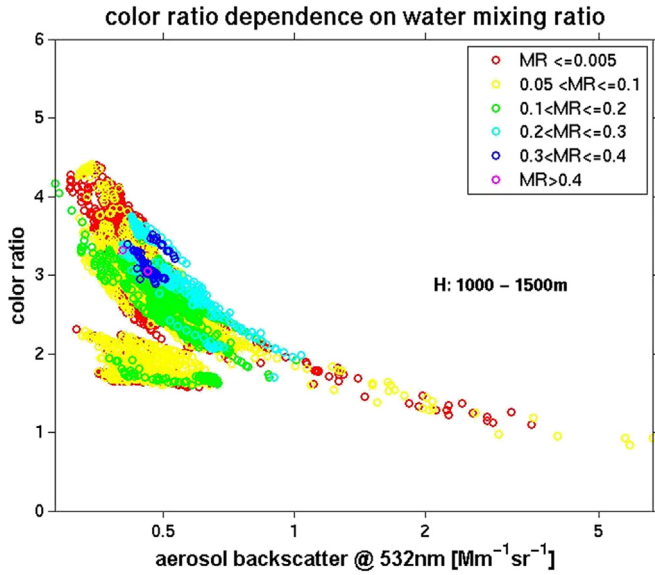


Fig. 33. Humidity dependent color ratio versus backscatter for the height interval 1–1.5 km. Units of the mixing ratio is [g/kg].

branch. These particles might therefore be remnants of a disintegrated liquid cloud. During the campaign we had 5 contemporary radio sonde launches parallel to lidar data and we do not find a correlation between the relative humidity and the backscatter or extinction coefficients. Hence, no clear (back-) scatter enhancement is observable for the majority of aerosol that was found in relative humidities between 15% and 70%. Therefore Fig. 33 should describe typical conditions. The clearly visible exceptions are the few cases of activated aerosol which will be discussed now.

One example for such a drying event is depicted in Figs. 34–36. They describe lidar measurements from 3 April. The radiosonde launched at UT 10:50 recorded almost 100% humidity in 1 km, still high humidity up to 1.4 km altitude and a cloud was present in this height. Some minutes later the sky cleared up and on UT 11:48 the lidar could be switched on. Fig. 34 shows the temporal evolution of the aerosol backscatter at 532 nm. A clear decrease on scale of 10 min can be seen. The data which refer to the activated aerosol, presented before, are marked by an asterisk symbol. (The profiles prior 12:34 had not been considered in the analysis before due to cloud screening – for this reason much more cases of activated aerosol may exist than described in this work). Note, that up to two hours after cloud disintegration still the activated aerosol with the described attributes did exist.

In Fig. 35 the lidar derived H₂O mixing ratios for the same period are presented. Only a small variability around 1 km can be seen, but at around 1.3 km altitude the drying of the air, as depicted by the lidar, is evident. Most important, however, is the implicit dependence of the mixing ratio on the temperature as the low (warm) atmosphere can hold more water vapor than the higher and colder layers.

Finally in Fig. 36 a rough estimation of the relative humidity is given. First, in black, the humidity profile from the RS-92 sonde at 10:50 UT is plotted. Next, the temperature profiles from the HATPRO radiometer have been linearly interpolated to the time-altitude mesh of the lidar. It was noted that in the temperature profile of the radiosonde at 1.4 km altitude at the cloud top a temperature inversion of 3 K depth was present, which was not visible in the radiometer. The overall temperature profile matched to the sonde well, but it was much too smooth. Therefore an error of 3 K in the temperature profile from the radiometer had to be

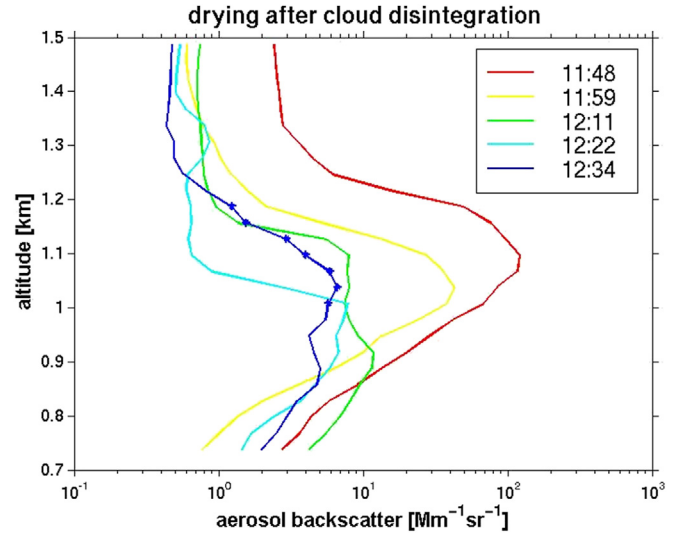


Fig. 34. Decrease of particle backscatter after the disintegration of a cloud.

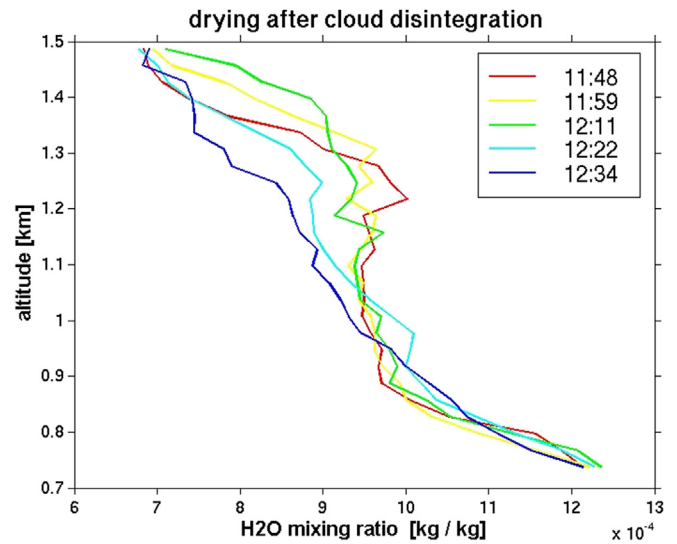


Fig. 35. Water vapor mixing ratio after the disintegration of a cloud.

considered and we assumed that the radiosonde captured the “true” temperature profile. Hence, for time t_0 we write for the temperature profile $T(z)$:

$$T_{sonde}(z, t_0) := T_{true}(z, t_0), \quad \Delta T(z) := T_{true}(z, t_0) - T_{HR}(z, t_0) \quad (4)$$

Where T_{HR} is the temperature profile from the HATPRO radiometer and z denotes to the height. For times t_i later than the balloon launch time t_0 we construct the true temperature profile estimations

$$T_{true}(z, t_i) = T_{HR}(z, t_i) - \Delta T(z) \quad (5)$$

In other words we assumed that the deviation between the HATPRO radiometer and the sonde (representing the true temperature profile) should be constant between times t_0 and t_i . To these temperature profiles $T_{true}(z, t_i)$ a constant error of ± 3 K was added. Finally from the mixing ratio in the lidar and the above introduced temperature profiles the relative humidities in Fig. 36

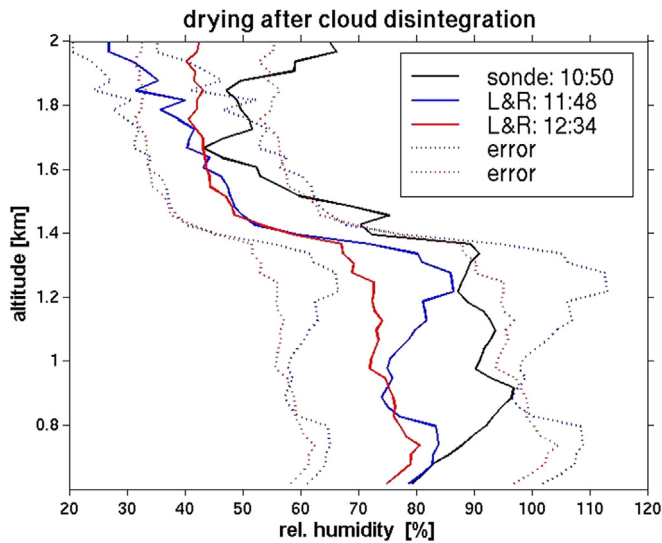


Fig. 36. Evolution of the rel. humidity. “L&R” stands for “lidar and radiometer”.

for times UT 11:48 and 12:34 were calculated. The 3 K insecurity in the temperature transfers into about 20% insecurity in the relative humidity (dotted lines in Fig. 36), but it seems as if the relative humidity would slowly decrease with time. Hence, if precise temperature profiles were available (back-) scatter enhancement factors could be derived from Raman lidar data (Zieger et al., 2011). Overall the decreasing values of backscatter and relative humidity over time support the hypothesis that a slow drying of droplets has been observed.

Generally over the campaign no pronounced temporal evolution has been observed, apart from the fact that at the end of the campaign and below 2 km altitude the lidar ratio decreased. At the beginning of the campaign the particles were slightly larger, which is typical for the haze season (Rastak et al., 2014). In 2–5 km altitude the particles seemed to be slightly more homogeneous in terms of distributions of depolarisation, color ratio and lidar ratio. This might indicate that effects of boundary layer properties or wind shear, acting on the aerosol in low altitudes, are less efficient in the free troposphere. Above 5 km altitude only very few larger, slightly elongated particles have been found.

Finally by inspecting the 850 hPa geopotential height and wind from ERA-Interim Reanalysis data set (Dee et al., 2011) for the periods prior to 14 April and after 22 April, which are shown in Fig. 37 and 38, one can speculate why the haze period might terminate by end April. It can be seen that the prevailing Northern wind, described earlier, results from a persistent low pressure system East of Spitsbergen. At the beginning of the iAREA campaign this system was quite strong and polluted air from East Asia might have been transported counter clockwise around it into the Eastern Arctic, the North pole and finally arrived at Spitsbergen. However, at the end of the campaign this low was weaker but more elongated towards the Laptev sea and the far Eastern air masses would have been deviated such that they arrive East of Spitsbergen, while our observing site was more influenced by a meandering flow from the central Arctic.

5. Conclusions

The main results of this work can be summarized like this:

- the spring season 2014 was considerably clear and sparse in long transport aerosol events. Sea salt and sulphate were identified as the main species

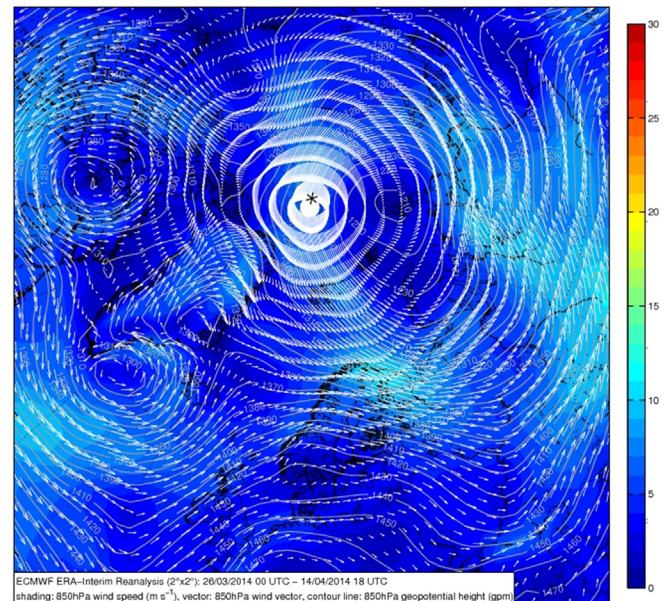


Fig. 37. Geopotential height and wind at 850 hPa averaged for 26 March – 14 April.

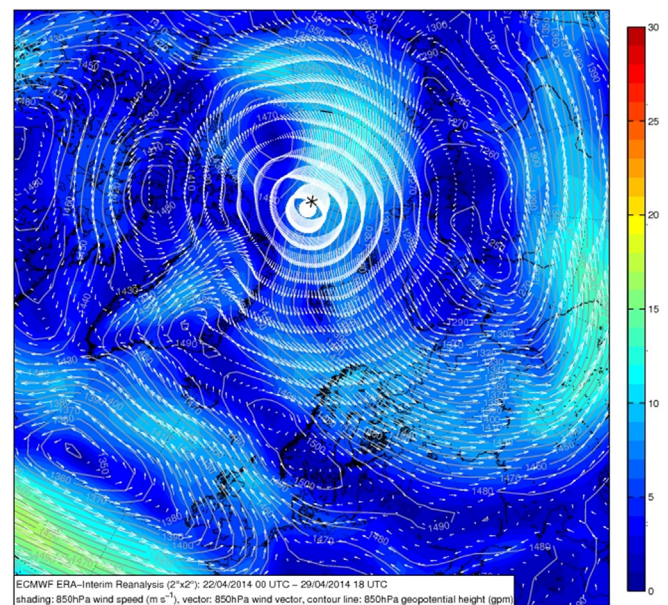


Fig. 38. Geopotential height and wind at 850 hPa averaged for 22 April – 29 April.

- typical values and its probability distribution of the aerosol backscatter, extinction, depolarisation, the lidar ratio and the color ratio which describe the aerosol properties during a 4 week campaign in the 2014 haze season have been presented.
- values of β^{aer} between 0.3 and 0.6 $\text{Mm}^{-1} \text{sr}^{-1}$ in 1–1.5 km for 532 nm have been typically found, which is a factor of 1.6 less than for the 2013 season
- lidar ratios between 30 and 50sr have been found, typically slightly lower LR for the 355 nm. At the end of the campaign the lidar ratio decreased at 355 nm and low altitudes. Hence, the assumption of one single value for the lidar ratio at a site as Ny-Ålesund can only be a rough estimation.

- values of aerosol depolarisation between 2 and 3% have been found, with slightly larger values at higher altitudes
- apart from the decrease of the lidar ratio and a slight decrease in particle size at the beginning of April no great temporal evolution has been observed, nevertheless generally the aerosol properties seemed to be more homogeneous above 2 km altitude. Even if our campaign only contains data of 5 weeks it seems as if the haze season might start earlier on the ground and lasts longer higher up. This effect is more visible in the extinction than in the backscatter
- no clear separation between particle size, particle shape and the lidar ratio has been found. This means that the chemical composition of the aerosol (in the given resolution 30 m, 10 min) does not depend on the particles size or shape. Especially no individual soot particles have been found
- the size of the particles is normally not correlated to humidity but directly determines the backscatter coefficient, contrary shape and chemical composition are not related to the backscatter
- a fair agreement between ground-based size distribution and chemical composition to the lidar data have been found.
- few large, spherical aerosol droplets with very low lidar ratios have been found after the disintegration of a cloud

Acknowledgements

Many thanks for the encouraged and great technical work at the AWIPEV station to Jürgen Graeser and Wilfried Ruhe.

References

- Ångström, A., 1929. On the atmospheric transmission of Sun radiation and on dust in the air. *Geogr. Ann.* 11, 156–166.
- Ansmann, A., Wandinger, U., Riebesell, M., Weitcamp, C., Michaelis, W., 1992. Independent measurement of extinction and backscatter profiles in cirrus clouds by using a combined Raman elastic-backscatter lidar. *Appl. Opt.* 31/33, 7113–7131. <http://dx.doi.org/10.1364/AO.31.007113>.
- Becagli, S., Ghedini, C., Peeters, S., Rottiers, A., Traversi, R., Udisti, R., Chiari, M., Jalba, A., Despiou, S., Dayan, U., Tamara, A., 2011. MBAS (methylene blue active substances) and LAS (linear alkylbenzene sulphonates) in mediterranean coastal aerosols: sources and transport processes. *Atmos. Environ.* 45, 6788–6801.
- Bowen, H.J.M., 1979. *Environmental Chemistry of the Elements*. Academic Press.
- Dee, D.P., Uppala, S.M., Simmons, A.J., Berrisford, P., Poli, P., Kobayashi, S., Andrae, U., Balmaseda, M.A., Balsamo, G., Bauer, P., Bechtold, P., Beljaars, A.C.M., van de Berg, L., Bidlot, J., Bormann, N., Delsol, C., Dragani, R., Fuentes, M., Geer, A.J., Haimberger, L., Healy, S.B., Hersbach, H., Holm, E.V., Isaksen, I., Kallberg, P., Kohler, M., Matricardi, M., McNally, A.P., Monge-Sanz, B.M., Morcrette, J.-J., Park, B.-K., Peubey, C., de Rosnay, P., Tavolato, C., Thepaut, J.-N., Vitart, F., 2011. The ERA-Interim reanalysis: configuration and performance of the data assimilation system. *Q. J. R. Meteorol. Soc.* 137, 553–597. <http://dx.doi.org/10.1002/qj.828>.
- Doherty, S.J., Anderson, T.L., Charlson, R.J., 1999. Measurement of the lidar ratio for atmospheric aerosols with a 180 degree backscatter nephelometer. *Appl. Opt.* 38 (9), 1823–1832.
- Ferrare, R.A., Turner, D.D., Heilman Brasseur, L., Feltz, W.F., Dubovik, O., Tooman, T.P., 2001. Raman lidar measurements of the aerosol extinction-to-backscatter ratio over the Southern Great Plains. *J. Geophys. Res.* 106, 20,333–20,347.
- Freudenthaler, V., Esselborn, M., Wiegner, M., Heese, B., Tesche, M., Ansmann, A., et al., 2009. Depolarization ratio profiling at several wavelengths in pure Saharan dust during SAMUM 2006. *Tellus B* 61B, 165–179. <http://dx.doi.org/10.1111/j.1600-0889.2008.00396.x>.
- Garrett, T.J., Brattström, S., Sharma, S., Worthy, D.E.J., Novelli, P., 2011. The role of scavenging in the seasonal transport of black carbon and sulfate to the Arctic. *Geophys. Res. Lett.* 38, L16805. <http://dx.doi.org/10.1029/2011GL048221>.
- Hoffmann, A., Ritter, C., Stock, M., Shiobara, M., Lampert, A., Maturilli, M., Orgis, T., Neuber, R., Herber, A., 2009. Ground-based lidar measurements from Ny-Ålesund during ASTAR 2007. *Atmos. Chem. Phys.* 9, 9059–9081. <http://dx.doi.org/10.5194/acp-9-9059-2009>.
- Hoffmann, A., 2011. Comparative Aerosol Studies Based on Multi-wavelength Raman LIDAR at Ny-Ålesund. Spitsbergen, PhD Thesis Uni. Potsdam. http://epic.awi.de/29932/1/Hof2011_g.pdf.
- Hoffmann, A., Osterloh, L., Stone, R., Lampert, A., Ritter, C., Stock, M., Tunved, P., Hennig, T., Böckmann, C., Li, S.-M., Eleftheriadis, K., Maturilli, M., Orgis, T., Herber, A., Neuber, R., Dethloff, K., 2012. Remote sensing and in-situ measurements of tropospheric aerosol, a PAMARCMIP case study. *Atmos. Environ.* <http://dx.doi.org/10.1016/j.atmosenv.2011.11>.
- Hogan, R.J., Illingworth, A.J., O'Connor, E.J., Póiresbaptista, J.P.V., 2003. Characteristics of mixed-phase clouds. II: a climatology from ground-based lidar. *Q. J. R. Meteorol. Soc.* 129, 2117–2134. <http://dx.doi.org/10.1256/qj.01.209>.
- Kerminen, V.-M., Teinilä, K., Hillamo, R., 2000. Chemistry of sea-salt particles in the summer Antarctic atmosphere. *Atmos. Environ.* 34, 2817–2825.
- Karasinski, G., Posyniak, M., Bloch, M., Sobolewski, P., Malarzewski, L., Soroka, J., 2014. Lidar observations of volcanic dust over polish polar station at Hornsund after Eruptions of Eyjafjallajökull and Grímsvötn. *Acta Geophys.* 62 (2), 316–339. <http://dx.doi.org/10.2478/s11600-013-0183-4>.
- Klett, J.D., 1981. Stable analytical inversion solution for processing lidar returns. *Appl. Opt.* 20 (2), 211–220. <http://dx.doi.org/10.1364/AO.20.000211>.
- Lisok, J., Markowicz, K.M., Ritter, C., Neuber, R., Makuch, P., Pakszys, P., Markuszewski, P., Petelski, T., Rozwadowska, A., Zielinski, T., Chilinski, M., Stachlewska, I.S., Becagli, S., Traversi, R., Udisti, R., Struzewska, J., Kaminski, J.W., Jefimow, M., 2016. Study of aerosol physical and chemical properties during iAREA2014 campaign on Spitsbergen. *Atmos. Environ.* (paper 1, in this issue).
- Miloshevich, L.M., Vömel, H., Whiteman, D.N., Leblanc, T., 2009. Accuracy assessment and correction of Vaisala RS92 radiosonde water vapor measurements. *J. Geophys. Res.* 114, D11305. <http://dx.doi.org/10.1029/2008JD011565>.
- Mishchenko, M.I., Travis, L.D., Kahn, R.A., West, R.A., 1997. Modeling shape functions for dustlike tropospheric aerosols using a shape mixture of randomly oriented polydisperse spheroids. *J. Geophys. Res.* 102, 16,831–16,847.
- Morganti, A., Becagli, S., Castellano, E., Severi, M., Traversi, R., Udisti, R., 2007. An improved flow analysis-ion chromatography method for determination of cationic and anionic species at trace levels in Antarctic ice cores. *Anal. Chim. Acta* 603, 190–198.
- Müller, D., Ansmann, A., Mattis, I., Tesche, M., Wandinger, U., Althausen, D., Pisani, G., 2007. Aerosol-type-dependent lidar ratios observed with Raman lidar. *J. Geophys. Res.* 112, D16202. <http://dx.doi.org/10.1029/2006JD008292>.
- Murayama, T., Okamoto, H., Kaneyasu, N., Kamataki, H., Miura, K., 1999. Application of lidar depolarization measurement in the atmospheric boundary layer: effects of dust and sea-salt particles. *JGR* 164 (D24), 31781–31792. <http://dx.doi.org/10.1029/1999JD900503>.
- Pakszys, P., Zielinski, T., Markowicz, K., Petelski, T., Makuch, P., Lisok, J., Chilinski, M., Rozwadowska, A., Ritter, C., Neuber, R., Udisti, R., Mazzola, M., 2015. Annual changes of aerosol optical depth and Ångström exponent over Spitsbergen. In: Zielinski, T., Weslawski, M., Kuliński, K. (Eds.), *Impact of Climate Changes on Marine Environments*, Book. Springer, pp. 23–36. ISBN: 978-3-319-14282-1.
- Pithan, F., Mauritsen, T., 2014. Arctic amplification dominated by temperature feedbacks in contemporary climate models. *Nat. Geosci.* 7, 181–184. <http://dx.doi.org/10.1038/ngeo2071>.
- Pornsawad, P., Böckmann, C., Ritter, C., Raffler, M., 2008. Ill-posed retrieval of aerosol extinction coefficient profiles from Raman lidar data by regularization. *Appl. Opt.* 47 (10), 1649–1661. <http://dx.doi.org/10.1364/AO.47.001649>.
- Quinn, P.K., Shaw, G., Andrews, E., Dutton, E.G., 2007. Arctic Haze: current trends and knowledge gaps. *Tellus B* 59, 99–114. <http://dx.doi.org/10.1111/j.1600-0889.2006.00238.x>.
- Rastak, N., Silvergren, S., Zieger, P., Wiedqvist, U., Ström, J., Svenningsson, B., Maturilli, M., Tesche, M., Ekman, A.M.L., Tunved, P., Riipinen, I., 2014. Seasonal variation of aerosol water uptake and its impact on the direct radiative effect at Ny-Ålesund. *Svalbard Atmos. Chem. Phys.* 14, 7445–7460. <http://dx.doi.org/10.5194/acp-14-7445-2014>.
- Rudnick, R.L., Gao, S., 2004. Composition of the continental crust. In: Rudnick, R.L. (Ed.), *The Crust*. In: Holland, H.D., Turckian, K.K. (Eds.), *Treatise in Geochemistry*, vol. 3. Elsevier Pergamon, Oxford.
- Screen, J.A., Simmonds, I., 2010. The central role of diminishing sea ice in recent Arctic temperature amplification. *Nature* 464, 1334–1337. <http://dx.doi.org/10.1038/nature09051>.
- Serre, M.C., Francis, J.A., 2006. The Arctic amplification debate. *Clim. Change* 76, 241–264. <http://dx.doi.org/10.1007/s10584-005-9017-y>.
- Shindell, D., Faluvegi, G., 2009. Climate response to regional radiative forcing during the twentieth century. *Nat. Geosci.* 2, 294–300. <http://dx.doi.org/10.1038/ngeo473>.
- Stachlewska, I., Ritter, C., 2010. On retrieval of lidar extinction profiles using two-stream and Raman techniques. *Atmos. Chem. Phys.* 10, 2813–2824. <http://dx.doi.org/10.5194/acp-10-2813-2010>.
- Stock, M., Ritter, C., Herber, A., von Hoyningen-Huene, W., Baibakov, K., Graeser, J., Orgis, T., Treffeisen, R., Zinoviev, N., Makshtas, A., Dethloff, K., 2012. Springtime Arctic aerosol: smoke versus haze, a case study for March 2008. *Atmos. Environ.* 52, 48–55. <http://dx.doi.org/10.1016/j.atmosenv.2011.06.051>.
- Stohl, A., 2006. Characteristics of atmospheric transport into the Arctic troposphere. *J. Geophys. Res.* 111, D11306. <http://dx.doi.org/10.1029/2005JD006688>.
- Stone, R.S., Anderson, G.P., Shettle, E.P., Andrews, E., Loukachine, K., Dutton, E.G., Schaaf, C., Roman, M.O., 2008. Radiative impact of boreal smoke in the Arctic: observed and modeled. *J. Geophys. Res.* 113, D14S16. <http://dx.doi.org/10.1029/2007JD009657>.
- Stone, R.S., Herber, A., Vitale, V., Mazzola, M., Lupi, A., Schnell, R.C., Dutton, E.G., Liu, P.S.K., Li, S.-M., Dethloff, K., Lampert, A., Ritter, C., Stock, M., Neuber, R., Maturilli, M., 2010. A three dimensional characterization of Arctic aerosols from airborne Sun photometer observations: PAM-ARCMIP, April 2009. *J. Geophys. Res.* 115, D13203. <http://dx.doi.org/10.1029/2009JD013605>.
- Stone, R.S., Sharma, S., Herber, A., Eleftheriadis, K., Nelson, D.W., 2014. A characterization of Arctic aerosols on the basis of aerosol optical depth and black

- carbon measurements. *Elementa: Sci. Anthropocene* 2 (1). <http://dx.doi.org/10.12952/journal.elementa.000027>, 000027.
- Tang, I.N., 1996. Chemical and size effects of hygroscopic aerosols on light scattering coefficients. *J. Geophys. Res.* 101 (D14), 19245–19250. <http://dx.doi.org/10.1029/96JD03003>.
- Tesche, M., Zieger, P., Rastak, N., Charlson, R.J., Glantz, P., Tunved, P., Hansson, H.-C., 2014. Reconciling aerosol light extinction measurements from spaceborne lidar observations and in situ measurements in the Arctic. *Atmos. Chem. Phys.* 14, 7869–7882. <http://dx.doi.org/10.5194/acp-14-7869-2014>.
- Toledano, C., Cachorro, V.E., Gausa, M., Stebel, K., Aaltonen, V., Berjón, A., Ortiz de Galisteo, J.P., Frutos, A.M., de Bennouna, Y., Blindheim, S., Myhre, C.L., Zibordi, G., Wehrli, C., Kratzer, S., Hakansson, B., Carlund, T., Leeuw, G. de, Herber, A., Torres, B., 2012. Overview of Sun photometer measurements of aerosol properties in Scandinavia and Svalbard. *Atmos. Environ.* 52, 18–28. <http://dx.doi.org/10.1016/j.atmosenv.2011.10.022>.
- Tomasi, C., Kokhanovsky, A.A., Lupi, A., Ritter, C., Smirnov, A., O'Neill, N.T., Stone, R.S., Holben, B.N., Nyeki, S., Wehrli, C., Stohl, A., Mazzola, M., Lanconelli, C., Vitale, V., Stebel, K., Aaltonen, V., de Leeuw, G., Rodriguez, Herber, A.B., Radionov, V.F., Zielinski, T., Petelski, T., Sakerin, S.M., Kabanov, D.M., Xue, Y., Mei, L., Istomina, L., Wagener, R., McArthur, B., Sobolewski, P.S., Kivi, R., Courcoux, Y., Larouche, P., Broccardo, S., Piketh, S.J., 2015. Aerosol remote sensing in polar regions. *Earth Sci. Rev.* 140, 108–157. <http://dx.doi.org/10.1016/j.earscirev.2014.11.001>.
- Udisti, R., Dayan, U., Becagli, S., Busetto, M., Frosini, D., Legrand, M., Lucarelli, F., Preunkert, S., Severi, M., Traversi, R., Vitale, V., 2012. Sea-spray aerosol in central Antarctica. Present atmospheric behavior and implications for paleoclimatic reconstructions. *Atmos. Environ.* 52, 109–120. <http://dx.doi.org/10.1016/j.atmosenv.2011.10.018>.
- Weitkamp, C. (Ed.), 2005. *Lidar, Range-resolved Optical Remote Sensing of the Atmosphere*. Springer series in optical sciences, ISBN 978-0-387-25101-1.
- Whiteman, D.N., Melfi, S.H., Ferrare, R.A., 1992. Raman lidar system for the measurement of water vapour and aerosols in the Earth's atmosphere. *Appl. Opt.* 31 (16), 3068–3082. <http://dx.doi.org/10.1364/AO.31.003068>.
- Yamanouchi, T., Treffeisen, R., Herber, A., Shiobara, M., Yamagata, S., Hara, K., Sato, K., Yabuki, M., Tomikawa, Y., Rinke, A., Neuber, R., Schumacher, R., Kriews, M., Ström, J., Schrems, O., Gernandt, H., 2005. Arctic study of tropospheric aerosol and radiation (ASTAR) 2000: Arctic haze case study. *Tellus B* 57, 141–157. <http://dx.doi.org/10.1111/j.1600-0889.2005.00140.x>.
- Zieger, P., Fierz-Schmidhauser, R., Gysel, M., Ström, J., Henne, S., Yttri, K.E., Baltensperger, U., Weingartner, E., 2010. Effects of relative humidity on aerosol light scattering in the Arctic. *Atmos. Chem. Phys.* 10, 3875–3890. <http://dx.doi.org/10.5194/acp-10-3875-2010>.
- Zieger, P., Weingartner, E., Henzing, J., Moerman, M., Leeuw, G.D., Mikkilä, J., Ehn, M., Petäjä, T., Clemer, K., Baltensperger, U., 2011. Comparison of ambient aerosol extinction coefficients obtained from in-situ, MAX-DOAS and LIDAR measurements at Cabauw. *Atmos. Chem. Phys.* 11 (6), 2603–2624. <http://dx.doi.org/10.5194/acp-11-2603-2011>.